



HAL
open science

Investigation of hydrothermal activity in the South West Indian ridge region using Ra isotopes and ^{227}Ac as tracers

Morgane Léon, Pieter van Beek, Virginie Sanial, Corentin Baudet, Matthew Charette, Marc Souhaut, Frédéric Vivier, Elodie Kestenare, Catherine Jeandel, Hélène Planquette

► To cite this version:

Morgane Léon, Pieter van Beek, Virginie Sanial, Corentin Baudet, Matthew Charette, et al.. Investigation of hydrothermal activity in the South West Indian ridge region using Ra isotopes and ^{227}Ac as tracers. *Progress in Oceanography*, 2024, 221, pp.103191. 10.1016/j.pocean.2023.103191. hal-04462046

HAL Id: hal-04462046

<https://hal.sorbonne-universite.fr/hal-04462046v1>

Submitted on 21 Nov 2024

HAL is a multi-disciplinary open access archive for the deposit and dissemination of scientific research documents, whether they are published or not. The documents may come from teaching and research institutions in France or abroad, or from public or private research centers.

L'archive ouverte pluridisciplinaire **HAL**, est destinée au dépôt et à la diffusion de documents scientifiques de niveau recherche, publiés ou non, émanant des établissements d'enseignement et de recherche français ou étrangers, des laboratoires publics ou privés.

1 **Investigation of hydrothermal activity in the South West Indian Ridge region**
2 **using Ra isotopes and ^{227}Ac as tracers**
3

4 **Morgane Léon¹, Pieter van Beek¹, Virginie Sanial², Corentin Baudet³, Matthew A.**
5 **Charette⁴, Marc Souhaut¹, Vivier Frédéric⁵, Kestenare Elodie¹, Catherine Jeandel¹, Hélène**
6 **Planquette³**

7 ¹ Laboratoire d'Etudes en Géophysique et Océanographie Spatiales (LEGOS), Université de
8 Toulouse, CNES/CNRS/IRD/Université Toulouse III Paul Sabatier (UT3), Toulouse, France

9
10 ² Université de Toulon, Aix Marseille Univ., CNRS, IRD, MIO, Toulon, France
11

12 ³CNRS, Univ Brest, IRD, Ifremer, LEMAR, F-29280, Plouzané, France.
13

14 ⁴Department of Marine Chemistry and Geochemistry, Woods Hole Oceanographic Institution,
15 Woods Hole, MA 02543, USA
16

17 ⁵LOCEAN-IPSL, CNRS, Sorbonne Université, Paris, France
18

19 Corresponding authors: Morgane Léon (morgane.leon@univ-tlse3.fr); Pieter van Beek
20 (pieter.van-beek@univ-tlse3.fr); Virginie Sanial (virginie.sanial@univ-tln.fr);

21 **Key Points:**

22 List **up to six key points** (at least one is required):
23

24 Radium isotopes, ^{227}Ac , SWIR, Hydrothermalism, Vertical eddy diffusivity coefficient,
25 Chemical fluxes

26 Abstract

27 Hydrothermal vents have been shown to be important vectors for various chemical
28 elements into the ocean. However, both the intensity of the chemical fluxes associated with these
29 systems and the fate of the chemical elements along the plume are still largely overlooked. At two
30 stations located above the South West Indian Ridge (SWIR), we investigate the distributions of
31 the Ra quartet (^{223}Ra , ^{224}Ra , ^{226}Ra and ^{228}Ra) and ^{227}Ac that have been used as tracers of
32 hydrothermal activity. While the vertical distributions of ^{226}Ra , ^{228}Ra and ^{227}Ac do not show a clear
33 enrichment at depth, unusual signatures of excess ^{223}Ra and ^{224}Ra near the seafloor are attributed
34 to the presence of a hydrothermal activity. The discrepancy observed between the different
35 isotopes is attributed to different chemical reactivity when seawater circulates within the crust
36 and/or to different regeneration rates within the fluid. A 1D diffusion model applied to the vertical
37 profiles of short-lived Ra isotopes provided an estimation of the vertical eddy diffusivity
38 coefficients (K_z) between $38 \text{ cm}^2 \text{ s}^{-1}$ and $149 \text{ cm}^2 \text{ s}^{-1}$. These high values suggest strong mixing
39 likely favored by the complex bathymetry in the region. By combining these K_z with the vertical
40 gradient of dissolved Fe (dFe), we estimate a vertical flux of dFe that ranges from 139 to 1173
41 $\text{nmol m}^{-2} \text{ d}^{-1}$. These results confirm that low-expansion-rate ridges could be significant sources of
42 dFe to the deep ocean.

43

44 1 Introduction

45 Since their discovery in the late 1970s (Corliss et al., 1979), hydrothermal vents have been
46 studied worldwide from biological, chemical and geological perspectives (Wolery and Sleep,
47 1976; Humphris et al., 1995; German and Von Damm, 2003; Baker et al., 2013). We distinguish
48 two main types of hydrothermal systems. At spreading ridges, magma chambers that contain
49 molten rock (basaltic and/or gabbroic) discharge lavas onto the ocean floor during volcanic
50 eruption events, producing black smokers and associated diffuse flows systems. Other
51 hydrothermal vents, known as mafic or ultramafic systems, are supplied by fault activities and
52 observed tens of kilometers off-axis (Martin et al. 2008).

53 When seawater percolates through the fractured oceanic crust, it interacts with the
54 surrounding rocks, which modifies significantly the seawater chemical composition
55 (Krishnaswami et al., 1982). For example, temperature, salinity, pH as well as the composition of
56 the solid phase control the partitioning of radionuclides from the U-Th series between the aqueous
57 and solid phases. While in marine systems radium (Ra) is easily released from surfaces or particles
58 due to the high ionic strength and is then found mostly in the dissolved phase, thorium (Th) and
59 protactinium (Pa) are strongly reactive to particles and preferentially adsorb onto mineral surfaces
60 (Cochran, 1982). ^{227}Ac is also believed to have a significant affinity for particles and may be
61 partially adsorbed onto mineral surfaces (Moore et al., 2008; Kipp et al., 2015), but due to its
62 higher solubility relative to Th and Pa, ^{227}Ac is partially released into the dissolved phase once it
63 is produced by the radioactive decay of ^{231}Pa (Anderson et al., 1983; Nozaki, 1984, 1993). Near
64 mid ocean ridges, radium activities increase in the dissolved phase in relationship with temperature
65 and the acidic nature of seawater (Edmond et al., 1979, 1982; Campbell et al., 1988; Kadko and
66 Moore, 1988; Kipp et al., 2015). Radium isotopes that display different half-lives (^{224}Ra , 3.66 days;

67 ^{223}Ra , 11.4 days; ^{228}Ra , 5.75 years; ^{226}Ra , 1600 years) have thus been widely used to trace
68 hydrothermal plumes (Kadko and Moore, 1988; Kadko, 1996; Kadko and Butterfield, 1998; Kadko
69 et al., 2007; Moore et al., 2008; Kipp et al., 2018; Neuholz et al., 2020a; Moore et al., 2021). ^{228}Ra ,
70 produced by the radioactive decay of ^{232}Th ($t_{1/2} = 1.405 \times 10^{10}$ years) is a preferred tracer to study
71 the crustal residence time of fluids (Kadko and Moore, 1988; Kadko, 1996; Kadko and Butterfield,
72 1998; Kadko et al., 2007). More recent studies used the short-lived isotopes, ^{223}Ra and ^{224}Ra -
73 produced by radioactive decay of ^{227}Ac ($t_{1/2} = 21.8$ years) and ^{228}Th ($t_{1/2} = 1.9$ years), respectively
74 - in order to constrain seawater residence time and trace element fluxes around hydrothermal vents
75 at shorter time scales (Kadko et al., 2007; Moore et al., 2008; Kipp et al., 2018; Neuholz et al.,
76 2020a; Moore et al., 2021). More specifically, Moore et al. (2008) were the first to observe high
77 activities of ^{223}Ra in excess of its parent ^{227}Ac in the low temperature hydrothermal vent system
78 of Puna Ridge (Hawaii, USA), thus demonstrating that ^{223}Ra was a powerful tracer of low-
79 temperature vents. Because of the particle affinity of ^{231}Pa and to a lesser extent of ^{227}Ac , the ^{227}Ac
80 activities observed in the vicinity of low temperature ridges are expected to be similar or even
81 lower than those in the ambient waters (Moore et al., 2008; Geibert et al., 2008). However, Kipp
82 et al. (2015) have shown that hydrothermal vents could be a source of this element to the deep
83 ocean and thus suggested that ^{227}Ac could be used as a tracer of these systems.

84 It is now well established that hydrothermal vents constitute significant vectors for various
85 gases and trace elements into the sea (Von Damm, 1990; Elderfield and Schultz, 1996; German
86 and Seyfried, 2014). In the vicinity of these systems, waters may be enriched in various chemical
87 elements and unique ecosystems develop (Ramirez-Llodra et al., 2010; Lemaitre et al., 2020). Fast
88 spreading ridges are thought to be important contributors to the oceanic iron inventory (e.g.,
89 Tagliabue et al., 2010) while slow spreading ridges have long been considered as less significant
90 and thus have been less explored, although they represent about half of the global mid ocean ridge
91 axis (Tagliabue et al., 2010). Interestingly, Saito et al. (2013) reported an upward revision of
92 estimated vent contribution of dissolved Fe (dFe) in the slow spreading rate Mid-Atlantic Ridge
93 and suggest that the ridge spreading rate is not the first order control of Fe flux from hydrothermal
94 vents. The impact of hydrothermal systems on the oceanic biogeochemical cycles depends not only
95 on the magnitude of the system, but also on the processes that control the persistence and the
96 transport of the chemical elements, which can extend thousands of km from the source, as was
97 shown for Fe (Resing et al., 2015; Tagliabue et al., 2022, Neuholz et al., 2020a,b). In the Southern
98 Ocean, inputs from the various hydrothermal vents to the surface may be favored by topography
99 upwelling features (Walter et al., 2010). However, the remoteness and extreme conditions of this
100 region complicate the investigation of hydrothermal vent localization and the fate of their plumes
101 (Ardyna et al., 2019). Because the Southern Ocean is the largest iron-limited region of the global
102 ocean, making phytoplankton highly sensitive to Fe inputs (Boyd and Ellwood, 2010), it was
103 proposed that upwelled hydrothermally influenced deep waters could promote phytoplankton
104 blooms in this region (Tagliabue et al., 2010; Ardyna et al., 2019; Schine et al., 2021). However,
105 Lough et al. (2023) highlight the complexity of tracing hydrothermal Fe supply due to uncertainties
106 associated with the at-sea sampling strategy and the temporal nature of plume dynamics. Hence it

107 is important to constrain the localization, the transport rate, as well as the fluxes of trace elements
108 and isotopes emanating from slow spreading ridge, especially in this region of the world's ocean.

109 The South West Indian Ridge (SWIR) is among the world's slowest spreading ridges with
110 a full spreading rate of $\sim 14\text{-}16 \text{ mm y}^{-1}$ (Patriat et al., 1997). To the present day, tens of active
111 hydrothermal vents have been identified along the SWIR, from the Westernmost part, off the coast
112 of South Africa (Baker et al., 2004), to the Easternmost part, off the coast of Madagascar (German
113 et al., 1998; Tao et al. 2009, 2014; Han et al. 2010; Liao et al., 2018). The presence of a
114 hydrothermal activity was suspected from a previous cruise conducted in the region between
115 Prince Edward (35°E) and Eric Simpson (40°E) fracture zones (SWIFT cruise, Jan-March 2001;
116 Humler et al., 2001). During this latter cruise, various geophysical data (bathymetry, magnetism
117 and gravity) were acquired along the ridge (Humler, 2001). Further, Sato et al. (2013) highlighted
118 magmatic activity in this region by conducting a geophysical survey between the Prince Edward
119 and Eric Simpson fracture zones (latitude 35 – 40° E). Following these previous studies, a detailed
120 bathymetric survey was conducted in this region of the SWIR during the SWINGS cruise and two
121 stations where hydrothermal activity was suspected were studied. In the present study, we
122 investigated the distribution of the four radium isotopes and ^{227}Ac at these two stations. Ra isotopes
123 and ^{227}Ac were used as tracers i) to investigate on the presence of a hydrothermal activity, ii) to
124 quantify the vertical eddy diffusivity coefficient K_z and iii) to estimate the vertical flux of dFe
125 associated with these systems.

126 2 Materials and Methods

127 2.1 Study area and geological settings

128 The SWINGS cruise took place on the R/V *Marion Dufresne* from January to March
129 2021 (<http://dx.doi.org/10.17600/18001925>) as part of the GEOTRACES program (GA01 section).
130 This cruise was designed to study the distribution of trace elements and isotopes in the Indian
131 sector of the Southern Ocean along a section between South Africa and Heard Island. Part of the
132 investigated transect was explored for bathymetry (see section 2.2.) and two stations (Station 14,
133 1388 m, 44°51.690 S, 36°10.460 E; Station 15, 1770 m, 44°51.178 S, 36°13.841 E) were studied
134 over the SWIR to investigate the presence of hydrothermal activity, following a previous cruise
135 that was conducted in this specific region (Humler, 2001).

136 The SWIR is a major plate boundary separating Africa and Antarctica for more than 100 Ma. The
137 ridge extends 7700 km from the Bouvet triple junction at 55° S, 1° W to the Rodrigues triple
138 junction at 26° S, 70° E and due to its ultra-slow spreading rate, the SWIR is one of the most rugged
139 topographies of all the world's ridges (DeMets et al., 1990). Based on magma supply, the SWIR
140 can be divided into three sections where several hydrothermal fields have already been discovered:
141 (i) the western region, located west of the Andrew Bain transform fault, which has a moderate
142 averaged magma supply, (ii) the middle region, located between Andrew Bain ($\sim 31^\circ\text{E}$) and
143 Gallieni ($\sim 52^\circ\text{E}$) transform fault, which has a strong averaged magma supply and (iii) the eastern
144 region, located east of the Gallieni transform fault, which has a weak averaged magma supply
145 (Sauter and Cannat, 2010; Tao et al., 2023). The middle region is overall hotter, has a thicker
146 oceanic crust and displays locally strong magma supply areas, discretely distributed along the
147 section (Tao et al., 2023). It has been shown that local enhanced magmatism promotes

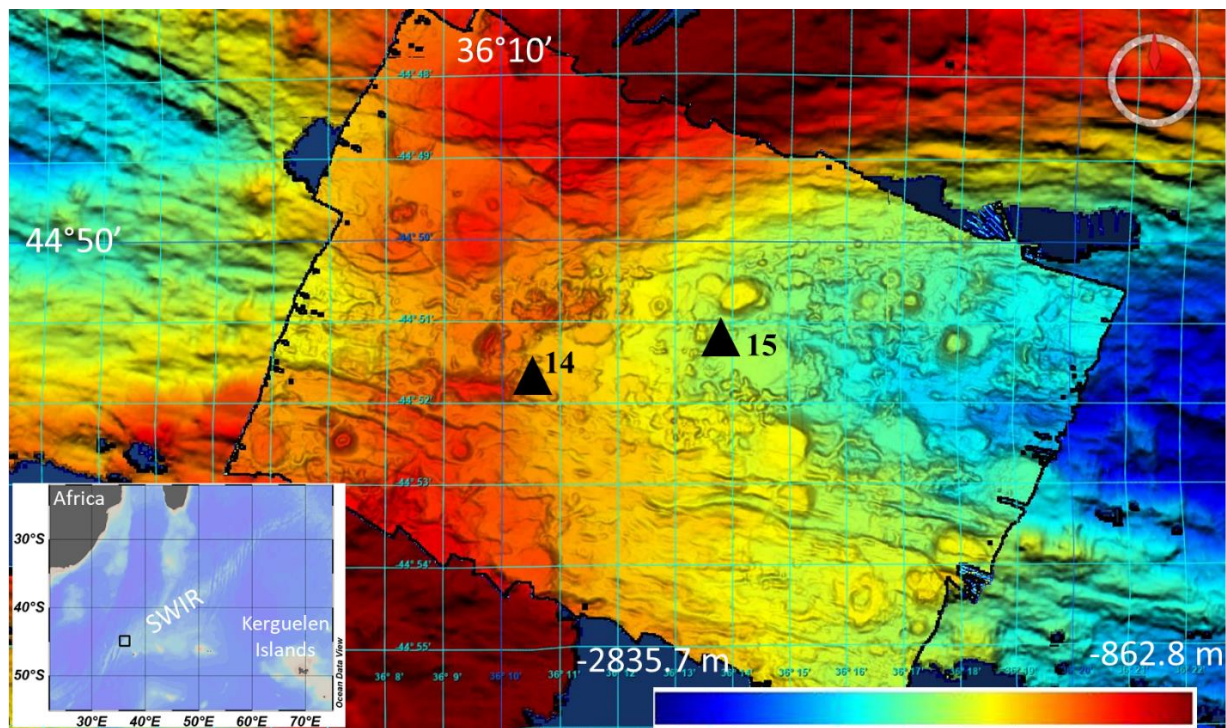
148 hydrothermal circulation (Tao et al., 2013; Chen et al., 2018). The Dunquiao hydrothermal field
149 located in the middle region - where stations 14 and 15 were investigated - is described as a typical
150 local strong magma supply hydrothermal field with intense magmatic activity (Tao et al. 2012).
151 A first cruise (SWIFT project, for South West Indian French Transect), initiated research in 2001
152 in the shallowest part of the SWIR between the Andrew Bain fracture zone and the Gallieni fracture
153 zone (middle section), using a multibeam sonar bathymetry gridded at 100 m (Humler, 2001;
154 <https://doi.org/10.17882/59494>). Through dredging of the seafloor - in the same area as station 14
155 investigated during the SWINGS project - pillow basalts, few pieces of ropey lava flows and traces
156 of biological activity were observed (e.g. at the SWIFT station DR05 located 44°51 S, 36°10 E,
157 1320 m). The section investigated here during the SWINGS project for bathymetry (see section
158 2.2) is part of a larger segment (PE-1) studied by Sato et al. (2013) who conducted geophysical
159 surveys including bathymetry, gravity and magnetism on the SWIR in the vicinity of the Marion
160 hotspot along several segments between Prince Edward and Eric Simpson fracture zones. Segment
161 PE-1 was shown to be dominated by local magma supply, similarly to the Dunquiao hydrothermal
162 field (50.5°E; Tao et al., 2012). Note that in the eastern part of the SWIR, other hydrothermal fields
163 such as Tiancheng (active, low temperature hydrothermal field) and Tianzuo (inactive
164 hydrothermal field) were also observed in magmatic zones (Chen et al., 2018; Tao et al. 2023). In
165 the PE-1 segment, the crust was estimated to be 7–8 km thick in the region investigated here (that
166 is, around the center of segment PE-1), the area of thick crust generally overlapping the area of
167 shallow topography. Sato et al. (2013) reported a mean spreading rate of segment PE-1 of 16.5
168 mm a⁻¹, which allows to classify the investigated region as an ultra-slow spreading ridge. Sato et
169 al. (2013) concluded that it may not be excluded that the magmatic activity of segments PE could
170 be influenced by the Marion hotspot. No specific geological observations were conducted during
171 the SWINGS cruise.

172

173 2.2 Bathymetric exploration

174

175 During the SWINGS cruise, a high-resolution (15 m) multibeam sonar bathymetric
176 exploration was performed during 25 hours above the SWIR on an area of approximately 200 km²
177 (Fig. 1; <https://doi.org/10.17882/89462>) between the prince Edward fracture zone and the Eric
178 Simpson fracture zone (36°05E to 36°21E). Data were acquired with a hull-mounted multibeam
179 echosounder Kongsberg EM122 12 kHz using an optimized configuration for bathymetry data
180 collection. Acoustic data were processed with the GLOBE software
181 (<https://doi.org/10.17882/70460>) to provide a 15 m resolution bathymetry map. The presence of a
182 consistent geomorphological feature (volcano shape) detected by the sonar survey has led to
183 further investigate both stations 14 and 15. The location of the two stations is reported on the high-
184 resolution bathymetric map (Fig. 1). The two stations are located on the flank of the ridge, about
185 5 km away from each other.



186
 187 **Figure 1.** High resolution (15 m) bathymetry map of the SWIR segment investigated during
 188 SWINGS cruise. The locations of stations 14 and 15 are shown as black triangles on the map. The
 189 location of the segment is shown on the bottom left panel (black square). The color bar shows the
 190 bathymetry that ranges from 862.8 to 2835.7 m.

191 2.3 Sampling method

192 Acrylic cartridges impregnated with MnO_2 (so called, Mn-cartridges) were prepared
 193 according to the protocol established by Henderson et al. (2013). These Mn-cartridges were
 194 mounted on McLane in-situ pumps (ISP) to preconcentrate dissolved Ra isotopes and ^{227}Ac from
 195 large volumes of seawater at various depths in the water column. Seawater first passed through
 196 Supor (0.8 μm pore size) or QMA (Whatman© 1 μm pore size) filters before passing through the
 197 Mn-cartridges. Eight ISP were deployed at station 14 and six ISP were deployed at station 15 for
 198 3 hours of pumping, thus filtrating through the Mn-cartridges between 427 and 677 L of seawater.
 199 Note that the sampling resolution was increased near the seafloor due to the expected presence of
 200 a hydrothermal activity. Except for the three shallowest pumps at station 14 (50 m, 200 m, 900
 201 m), two Mn-cartridges were mounted in series in order to provide information on the yield of ^{227}Ac
 202 fixation, following Henderson et al. (2013) and Le Roy et al. (2019).

203 Water samples were also collected from Niskin bottles (ca. 12 L) mounted on a rosette and
 204 deployed at the same depths as the ISPs. These samples were designed to collect dissolved ^{226}Ra .
 205 Because ^{226}Ra displays higher activities in seawater than ^{223}Ra , ^{224}Ra and ^{228}Ra , the analysis of
 206 ^{226}Ra can be conducted in relatively small volumes ($\sim 10\text{-}12$ L). These samples were then passed
 207 by gravity through 10 g of acrylic fibers impregnated with MnO_2 (so called, Mn-fibers) at a flow
 208 rate < 0.5 $\text{L}\cdot\text{min}^{-1}$ to quantitatively adsorb ^{226}Ra isotopes. By doing so, we assume that the Mn-
 209 fibers scavenge 100% of Ra (Moore and Reid, 1973).

210 To sample dissolved iron (dFe), GO-FLO bottles were mounted on a trace metal clean
 211 rosette. All manipulations of the GO-FLO bottles occurred into a clean container dedicated for

212 sampling trace elements. Seawater was filtered on-line through a 0.45 μm polyethersulfone filter
213 (Supor) and collected in acid-cleaned 60 mL LDPE bottles. The samples were then acidified within
214 24h after collection with HCl (ultrapure grade, Merck, final pH 1.8) (Baudet et al., submitted).
215

216 2.4 Analytical method

217
218 Both Mn-cartridges and Mn-fibers were analyzed using four Radium Delayed Coincidence
219 Counter (RaDeCC) systems (Moore, 2008). All samples were analyzed for 6 to 24 hours by
220 flushing the RaDeCC system every 3 hours during 5 to 10 minutes with air, before reintroducing
221 helium into the system. Because of their short half-life, ^{224}Ra and ^{223}Ra were measured on board,
222 within a few hours of sample collection. This first measurement provides the total ^{224}Ra ($^{224}\text{Ra}_{\text{tot}}$)
223 and ^{223}Ra ($^{223}\text{Ra}_{\text{tot}}$) activities. A second measurement was conducted 21 days after sampling, to
224 quantify the ^{224}Ra supported by ^{228}Th in the samples. These supported activities were then
225 subtracted from the $^{224}\text{Ra}_{\text{tot}}$ activities to determine excess ^{224}Ra (denoted $^{224}\text{Ra}_{\text{ex}}$). A third counting
226 was performed about 90 days after sample collection to quantify the ^{223}Ra supported by ^{227}Ac . In
227 the same way, these supported activities were then subtracted from the $^{223}\text{Ra}_{\text{tot}}$ activities to
228 determine excess ^{223}Ra (denoted $^{223}\text{Ra}_{\text{ex}}$). In the following, the activities reported for short-lived
229 Ra isotopes are thus $^{223}\text{Ra}_{\text{ex}}$ and $^{224}\text{Ra}_{\text{ex}}$. Error propagation calculations followed Garcia-Solsona
230 et al. (2008). RaDeCCs were calibrated with Mn-cartridges and Mn-fibers impregnated with ^{232}Th
231 standards. The detection efficiencies of the RaDeCCs for ^{223}Ra and ^{227}Ac were determined
232 following Moore and Cai, (2013). In order to quantify ^{227}Ac , between 3 and 5 analyses were
233 performed for each sample using RaDeCC and the ^{227}Ac activities reported here correspond to the
234 mean of these different analyses (Léon et al., in prep.). The yield of ^{227}Ac fixation onto the Mn-
235 cartridges was determined from the two Mn-cartridges placed in series, as was done in the past for
236 various radionuclides (Mann and Casso, 1984; Livingston and Cochran, 1987; Baskaran et al.,
237 1993; van der Loeff and Moore, 1999; Le Roy et al., 2019). Errors reported for the ^{227}Ac activities
238 correspond to the standard deviation of the mean (1SD).

239 The analyses of the ^{226}Ra activities on Mn-fibers were performed using a ^{222}Rn extraction
240 line (daughter of ^{226}Ra , half-life: 3.8 days) followed by alpha scintillation counting system.
241 Briefly, the Mn-fibers are first placed in PVC cartridges (Peterson et al., 2009) and then flushed
242 with helium for five minutes at a flow rate of 250 min L^{-1} . These cartridges are then sealed and
243 held about one week (minimum of 5 days) before being analyzed to await radioactive regrowth of
244 ^{222}Rn . The ^{222}Rn is then flushed out of the cartridge and cryo-trapped in a copper tube cooled with
245 liquid nitrogen. After about 15 minutes of ^{222}Rn accumulation in the copper tube, the copper tube
246 was heated and the ^{222}Rn was guided by helium into a Lucas cell, an airtight chamber covered with
247 silver activated zinc sulfide on its inner walls which emit a photon when struck by an alpha particle
248 (Key et al., 1979; Lucas, 1979; Peterson et al., 2009). The analysis of these cells takes place 3h
249 after sealing in order to reach the secular equilibrium of the ^{222}Rn daughters. Cells are counted for
250 several hours (from 3 to 6 hours) in a Rn counting system (model AC/DC-DRC-MK 10-2).
251 Uncertainties reported for ^{226}Ra include counting statistics and uncertainty on the detection
252 efficiencies (1SD).

253 The analyses of the ^{226}Ra activities on Mn-cartridges were performed using a large, low
254 background, high efficiency, well-type germanium gamma spectrometer (SAGe-Well, MIRION-
255 CANBERRA) placed underground at the LAFARA laboratory in the French Pyrénées. The volume
256 of the germanium crystal is 450 cm^3 and the diameter of the well is 32 mm. The facility is located

257 under 85 m of rock that protect the detectors from cosmic radiations, thus providing a very low
258 background (van Beek et al., 2013). Prior to analysis, Mn-fibers were pressed into plastic tubes
259 while Mn-cartridges were ashed (to reduce the volume) before being placed in the tubes. The tubes
260 were then sealed to prevent any loss of ^{222}Rn from the samples and were analyzed 3 weeks after
261 the sample preparation to make sure that radioactive equilibrium is reached between ^{226}Ra , ^{222}Rn
262 and the following daughters. ^{226}Ra activities were determined using the ^{214}Pb (295 keV and 352
263 keV) and ^{214}Bi (609 keV) peaks after 5 days of counting. We used the APEX software (MIRION-
264 CANBERRA) to quantify these activities. Uncertainties reported for ^{226}Ra include counting
265 statistics and uncertainty on the detection efficiencies (1SD).

266 Here, we report $^{223}\text{Ra}_{\text{ex}}/^{226}\text{Ra}$, $^{224}\text{Ra}_{\text{ex}}/^{226}\text{Ra}$, $^{228}\text{Ra}/^{226}\text{Ra}$ and $^{224}\text{Ra}_{\text{ex}}/^{228}\text{Ra}$ ratios determined
267 in Mn-cartridges (Table 1). By combining these ratios with the ^{226}Ra activities determined using
268 Mn-fibers (that quantitatively remove Ra from seawater), we could determine $^{223}\text{Ra}_{\text{ex}}$, $^{224}\text{Ra}_{\text{ex}}$ and
269 ^{228}Ra activities in the water columns at stations 14 and 15. The vertical profiles of ^{227}Ac activities
270 were built by analyzing ^{227}Ac in Mn-cartridges placed in series, following the protocol described
271 in Le Roy et al. (2019).

272 In order to analyze the total dFe concentrations, samples were stored at room temperature
273 and measured at LEMAR in Brest, 12 months after sampling. dFe concentrations were analyzed
274 using a preconcentration system seaFAST-picoTM coupled to a high-resolution magnetic sector
275 field inductively-coupled plasma mass spectrometer (SF-ICP-MS, Element XR – Pôle
276 Spectrométrie Océan, Brest) following Tonnard et al., (2020). An air blank (no sample uptaken
277 but with contribution of all reagents) of $0.14 \pm 0.05 \text{ nmol L}^{-1}$ was used. The vertical profiles of
278 dFe can be found in Baudet et al. (submitted).

279

280 2.5 Ancillary data

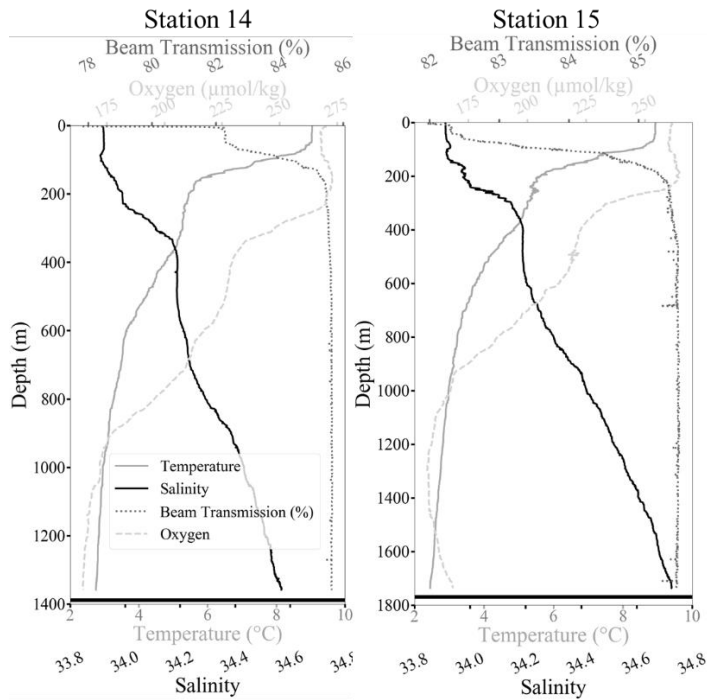
281 Hydrographic profiles were collected with a Seabird SBE911plus conductivity-
282 temperature-depth (CTD) probe with an accuracy of $\pm 0.001^\circ \text{ C}$ for temperature and $\pm 0.003 \text{ mS/cm}$
283 for conductivity. Dissolved oxygen concentration was measured with a Seabird SBE43 sensor
284 attached to the rosette. Oxygen data were further calibrated with ex-situ titrations (Winkler
285 method) from water samples taken at stations regularly spaced during the cruise. Beam
286 transmittance was measured with a WET Labs C-Star transmissometer. Velocity profiles were
287 collected at each station from a pair of lowered-acoustic Doppler current profilers (LADCP)
288 mounted on the rosette, composed of an up-looking and a down-looking Workhorse Sentinel
289 ADCP from Teledyne RD Instruments operating at 300 kHz and 150 kHz, respectively. LADCP
290 data were processed based on the velocity inversion method (Visbeck, 2002) using the IFM-
291 GEOMAR/LDEO software (Visbeck and Krahnemann, version 11.0). Other ancillary data include
292 daily altimeter satellite gridded sea-surface height and derived surface geostrophic currents at
293 0.25° spatial resolution from the Copernicus Marine Environment Monitoring Service (CMEMS),
294 and daily horizontal current fields at 46 vertical levels from the state-of-the-art GLORYS12 global
295 eddy-resolving ocean and sea ice reanalysis at $1/12^\circ$ horizontal resolution implemented in the
296 framework of the CMEMS (Lellouche et al 2021). GLORYS12 assimilates a variety of
297 observations including satellite sea level anomaly, surface temperature and sea ice concentration,
298 as well as available hydrographic in situ data. Barotropic tidal currents were estimated separately
299 with the Tide Model Driver (TMD v2.5) package developed by Earth and Space Research, using
300 the TPXO9v5 global tide model with 14 harmonic constituents, assimilating satellite altimeter data
301 (Egbert and Erofeeva, 2002).

302 **3 Results**

303 3.1. Hydrography and circulation above the SWIR

304 The vertical profiles of temperature, salinity, beam transmission and oxygen are reported
305 in Fig 2. For both stations, the temperature decreased rapidly over the first 200 meters and then
306 more slowly from about 5°C to 2-3°C near the bottom. Salinity increases almost constantly with
307 depth, with notably a high increase from around 300 m. Beam transmission, which can reflect the
308 presence of particulate matter, increases away from the surface and then stabilizes at a value close
309 to 85.5% along the vertical profiles. The O₂ concentration remains almost stable from the surface
310 to 200 m (~270 $\mu\text{m.kg}^{-1}$), then decreases regularly up to 1000 m where it reaches approximately
311 170 $\mu\text{m.kg}^{-1}$ near the bottom. Except for a slight increase (0.02) of salinity at station 14 in 70 m
312 thick bottom boundary layer, no clear pattern was observed in salinity, temperature, O₂ or beam
313 transmission that could indicate the presence of a hydrothermal activity at these two stations (Fig.
314 2). Temperature and salinity observed here suggest a surface mixed layer of about 100 m at Station
315 14 and about 70 m at station 15. The different water masses encountered were identified. The
316 Antarctic Intermediate Water (AAIW), characterized by temperature between 0 and 5°C and
317 salinity about 33.5 - 34.5, was found down to 800 m. The Circumpolar Deep Water (CDW), with
318 a neutral density larger than 27.5 kg m^{-3} , lies just below the AAIW layer and can be decomposed
319 into (i) Upper Circumpolar Deep Water (UCDW) and (ii) Lower Circumpolar Deep Water
320 (LCDW), which was found at depths greater than 1350 m (station 15). The stations were too

321 shallow to observe Antarctic Bottom Water (AABW), usually present below 3000 m (Park and
 322 Gamberoni, 1997).

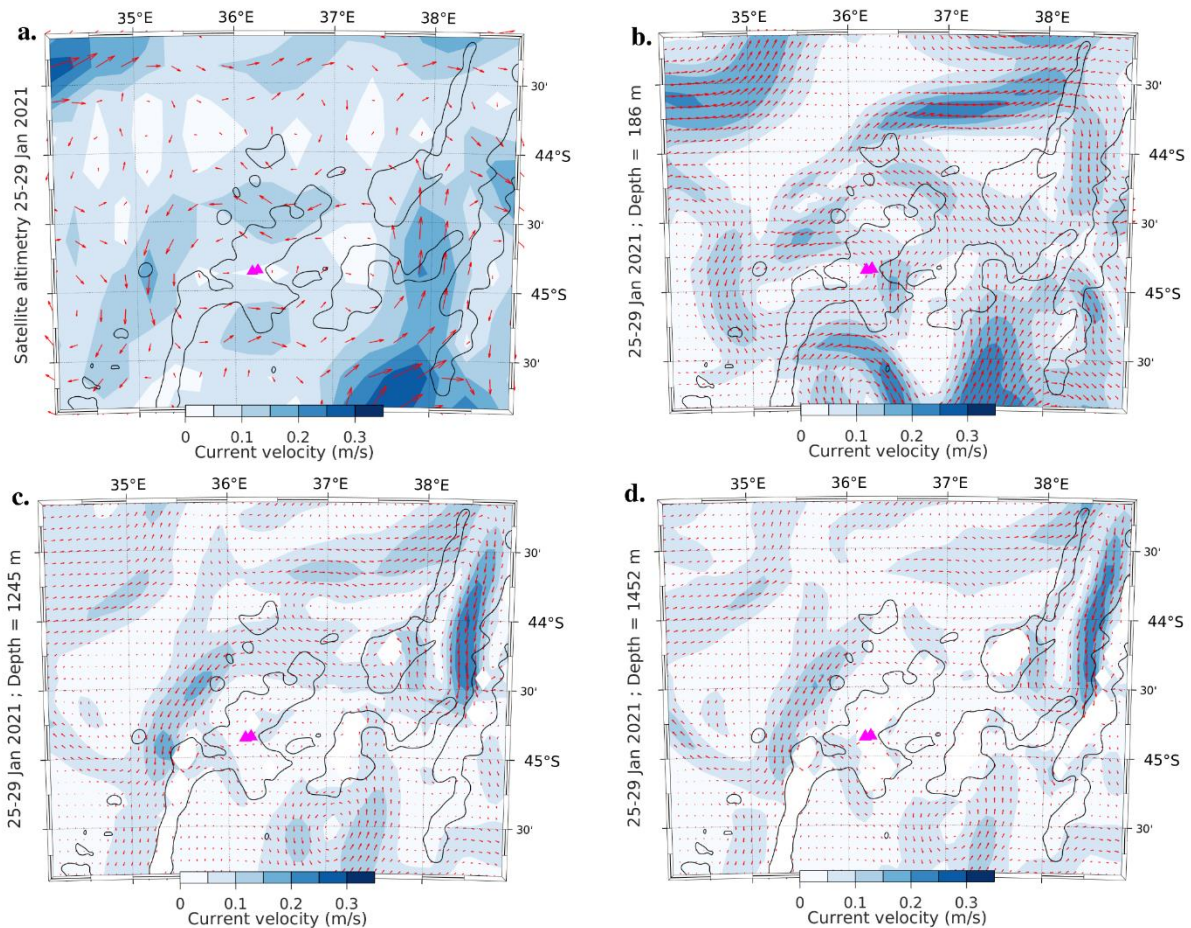


323

324 **Figure 2:** Temperature (grey full line), salinity (black full line), beam transmission (black dotted
 325 line) and oxygen (grey dashed line) profiles at stations 14 (left panel) and 15 (right panel). The
 326 horizontal black lines represent the bottom depth for each station.

327 The concurrent surface geostrophic velocity field derived from satellite altimetry
 328 averaged between 25 and 29 January (Fig. 3a) indicates that the study area was away from the
 329 fronts and deep-reaching jets associated with the Antarctic Circumpolar Current: stations 14 and
 330 15 were located at the center of a weak anticyclonic circulation pattern straddling the ridge, a
 331 location associated with a low velocity ($< 5 \text{ cm s}^{-1}$). The horizontal velocity field at successive
 332 depths is provided by the GLORYS12 reanalysis (Fig. 3b-d). The latter was assessed by comparing
 333 the velocity field at 190 m depth, i.e., below the Ekman layer, with the surface geostrophic velocity
 334 field from altimetry, demonstrating a reasonable agreement in the region of interest with, however,
 335 a slight westward shift of the anticyclonic circulation pattern mentioned above (Fig. 3b). Below

336 1000 m depth, horizontal currents at stations 14 and 15 are smaller than at the near surface, but
 337 remain consistently northeastwards (Fig. 3c-d).

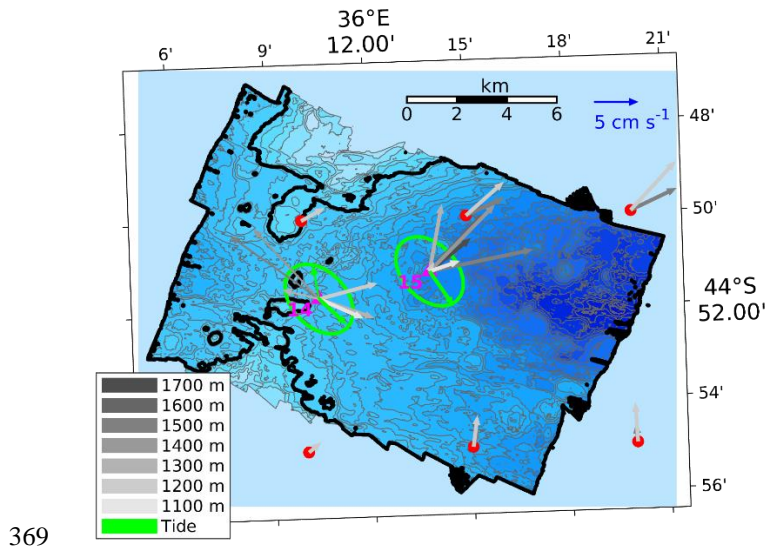


338

339 **Figure 3.** Map of horizontal currents averaged between January 25 and January 29, 2021, from
 340 satellite altimetry (a.) and from the GLORYS12 reanalysis at 190 m (b), 1250 m (c) and 1450 m
 341 (d). The black line denotes the 2000 m isobath. The location of stations 14 and 15 is indicated by
 342 magenta triangles. Units in m s^{-1} .

343 Focusing on a domain of a few kilometers around the stations, the GLORYS12 currents
 344 below 1000 m depth for 28 January 2021 are reported in Fig. 4, together with those measured on
 345 station. Two LADCP casts were performed at station 14 (28 January, 17h UTC and 21h UTC)
 346 whereas only one was performed for station 15 on 29 January 17h UTC. The two casts at station
 347 14 provide an appreciation of the importance of tidal currents, with nearly opposing directions at
 348 a 4h interval. This reversal of currents at station 14 is roughly consistent with the modeled
 349 barotropic tidal currents according to TPXO9v5 (green arrows). The principal lunar semidiurnal
 350 M2 constituent overwhelmingly dominates, accounting for 99% of the tidal current variance for
 351 the period ranging from 27 January to 2 February. The corresponding M2 tidal ellipses are slightly
 352 stretched along a southeast-northwest axis (Fig. 4), and identical between station 14 and 15,
 353 although the influence of local topography seems to be important as evidenced by the preferential
 354 direction of LADCP currents across the saddle point of the ridge, west of station 14. The effective

355 resolution of the TPXO9 atlas of tidal constituents is $1/6^\circ$ (>18 km) away from coastal regions
 356 while the provided map resolution is $1/30^\circ$; therefore, the fine scales of the flow associated with
 357 the local bathymetry cannot be resolved. At station 15, the LADCP current below 1000 m depth
 358 is northeastward, consistent, albeit larger, with the velocity field from the GLORYS12 simulation,
 359 which does not include tides. Note that GLORYS12 currents were nearly constant over the few
 360 days preceding *in-situ* measurements. We conclude from this analysis that horizontal currents
 361 below 1000 m depth include a substantial contribution from the semidiurnal tide, on the order of
 362 5 cm s^{-1} or more at station 14 where it appears to be the dominant signal. Superimposed on tidal
 363 currents, the GLORYS12 simulation features a smaller constant northeastward flow, that seems
 364 topographically guided along the ridge. This current is increasingly larger to the east according to
 365 GLORYS12 reaching $\sim 5 \text{ cm s}^{-1}$ at station 15, where its direction is consistent with LADCP data,
 366 but also with the slope of isopycnals between stations 14 and 15 (not shown). The differences
 367 between LADCP data and model can be explained by many factors, which include, besides tides,
 368 the high-frequency/small-scale dynamics that are not resolved.



370 **Figure 4.** Horizontal currents at depths below 1000 m measured by the LADCP at station 14 on
 371 28 January 2021 and at station 15 on 29 January. A second LADCP cast was performed at station
 372 14 on 28 January, denoted by thin arrows. Green arrows denote the barotropic tidal current at the
 373 time of the cast according to the TPXO9v5 model. Corresponding variance ellipses for the
 374 dominant M2 constituent computed between 27 January and 2 February are also shown. Current
 375 velocity on 28 January from the GLORYS12 reanalysis are shown at a depth of 1250 m and 1450
 376 m (where applicable): red dots denote model grid points. Bathymetry is from the multibeam echo
 377 sounder (contour interval 50 m), with the 1250 m isobath highlighted. Unit for the velocity is cm
 378 s^{-1} (velocity scale in the top right corner).

379 3.2. Ra isotopes and ^{227}Ac activities above the SWIR

380 **Table 1:** Radium activities at stations 14 and 15, “<DL” indicates activities below detection limit. Here we report i) the Ra activity
 381 ratios determined in Mn-cartridges, ii) Ra activities determined using Mn-fibers and iii) Ra activities in seawater determined by
 382 combining the ^{226}Ra activities determined using Mn-fibers and the activity ratios determined using Mn-cartridges.

383

Station	Depth Volume		Activity ratios (Mn-cartridges)				Depth Volume		Activities (Mn-fibers)			Activities (seawater)		
	(m)	(L)	$^{228}\text{Ra}/^{226}\text{Ra}$	$^{223}\text{Ra}_{\text{ex}}/^{226}\text{Ra}$	$^{224}\text{Ra}_{\text{ex}}/^{226}\text{Ra}$	$^{224}\text{Ra}_{\text{ex}}/^{228}\text{Ra}$	(m)	(L)	$^{223}\text{Ra}_{\text{ex}}$ dpm 100L ⁻¹	$^{224}\text{Ra}_{\text{ex}}$ dpm 100L ⁻¹	^{226}Ra dpm 100L ⁻¹	^{228}Ra dpm 100L ⁻¹	$^{223}\text{Ra}_{\text{ex}}$ dpm 100L ⁻¹	$^{224}\text{Ra}_{\text{ex}}$ dpm 100L ⁻¹
14	50	427	0.026 ± 0.007	<DL	0.001 ± 0.0006	0.04 ± 0.02	50	11.9			11.11 ± 0.30	0.29 ± 0.08	<DL	0.01 ± 0.01
	200	601	0.024 ± 0.007	<DL	0.002 ± 0.0006	0.09 ± 0.04	202	12.7			13.17 ± 0.23	0.31 ± 0.09	<DL	0.03 ± 0.01
	900	615	<DL	<DL	<DL	<DL	910	12.7			15.26 ± 0.63	<DL	<DL	<DL
	1000	528	0.009 ± 0.005	0.015 ± 0.0007	<DL	0.02 ± 0.07	1011	11.9			17.27 ± 0.84	0.16 ± 0.08	0.25 ± 0.02	<DL
	1100	548	0.014 ± 0.004	0.021 ± 0.0008	0.003 ± 0.0005	0.22 ± 0.08	1112	11.8			15.48 ± 0.43	0.22 ± 0.07	0.33 ± 0.02	0.05 ± 0.01
	1150	584	0.008 ± 0.004	0.038 ± 0.0012	0.004 ± 0.0004	0.47 ± 0.21	1162	11.9			14.18 ± 0.66	0.12 ± 0.05	0.53 ± 0.03	0.06 ± 0.01
	1200	674	0.010 ± 0.004	0.078 ± 0.0009	0.011 ± 0.0006	1.10 ± 0.44	1213	12.0		0.21 ± 0.16	16.78 ± 0.18	0.16 ± 0.06	1.30 ± 0.02	0.18 ± 0.01
	1250	646	0.014 ± 0.005	0.164 ± 0.0013	0.018 ± 0.0007	1.32 ± 0.44	1265	11.9			15.49 ± 0.32	0.22 ± 0.07	2.54 ± 0.06	0.28 ± 0.01
	1300						1311	11.8			17.74 ± 0.19			
	1340						1353	11.8	3.16 ± 2.21	0.69 ± 0.18	16.63 ± 0.88			
	1360						1370	11.9	1.93 ± 1.84	0.47 ± 0.18	16.01 ± 0.65			
15	700	532	<DL	<DL	<DL	<DL						<DL	<DL	<DL
	1160	579	0.009 ± 0.005	0.009 ± 0.0004	0.001 ± 0.0004	0.16 ± 0.09	1174	11.2		1.05 ± 0.23	15.84 ± 0.36	0.15 ± 0.08	0.14 ± 0.01	0.02 ± 0.01
	1200	503	0.014 ± 0.005	0.005 ± 0.0008	0.002 ± 0.0004	0.16 ± 0.06	1216	11.6		0.37 ± 0.18	16.57 ± 0.34	0.22 ± 0.08	0.09 ± 0.01	0.03 ± 0.01
	1260	665	0.007 ± 0.003	0.010 ± 0.0008	0.010 ± 0.0004	1.48 ± 0.66	1275	11.4			17.51 ± 0.93	0.12 ± 0.05	0.17 ± 0.02	0.18 ± 0.01
	1370	677	0.011 ± 0.005	0.013 ± 0.0011	0.002 ± 0.0004	0.22 ± 0.11	1383	11.3			16.19 ± 0.32	0.17 ± 0.08	0.20 ± 0.02	0.04 ± 0.01
	1500						1519	21.8		0.15 ± 0.10	17.20 ± 0.12			
	1690	630	0.017 ± 0.004	0.296 ± 0.0031	0.049 ± 0.0011	2.91 ± 0.73	1708	11.2	7.05 ± 2.90		17.41 ± 0.31	0.30 ± 0.07	5.15 ± 0.11	0.86 ± 0.02
	1755						1755	11.5	5.28 ± 2.72	0.98 ± 0.20	17.32 ± 0.26			

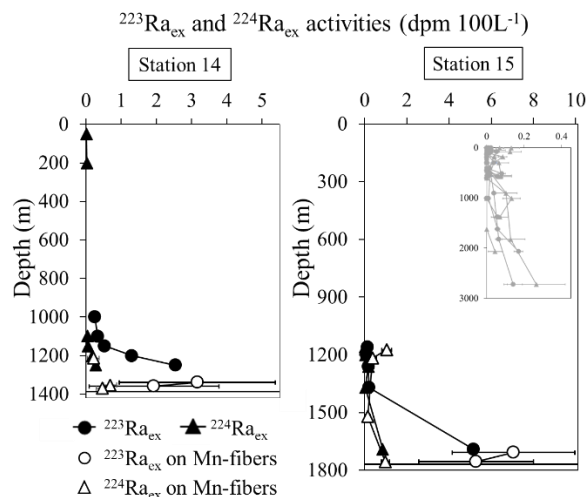
384

385 **Table 2:** ^{227}Ac activities, in dpm 100L^{-1} , at stations 14 and 15.

Station	Depth (m)	^{227}Ac
		(dpm 100L^{-1})
14	50	0.023 ± 0.008
	210	0.016 ± 0.006
	900	0.018 ± 0.007
	1000	0.035 ± 0.011
	1100	0.026 ± 0.013
	1160	0.020 ± 0.008
	1200	0.035 ± 0.010
	1260	0.034 ± 0.012
15	700	0.018 ± 0.012
	1160	0.028 ± 0.003
	1200	0.033 ± 0.011
	1260	0.038 ± 0.004
	1370	0.034 ± 0.004
386	1690	0.054 ± 0.007

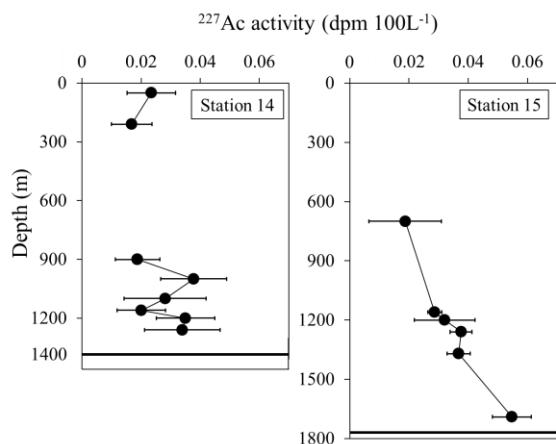
387 The activities of radium isotopes ($^{223}\text{Ra}_{\text{ex}}$, $^{224}\text{Ra}_{\text{ex}}$, ^{226}Ra , ^{228}Ra) are reported in Table 1
388 and the vertical profiles of $^{223}\text{Ra}_{\text{ex}}$ and $^{224}\text{Ra}_{\text{ex}}$ activities are shown in Fig. 5. For both isotopes, we
389 observe very low activities in surface waters at station 14 (< 0.03 disintegration per minute per
390 100L ; dpm 100L^{-1}) and activities below the detection limit at 900 m. Activities then increase with
391 increasing depth and reach values up to 0.69 dpm 100L^{-1} and 3.16 dpm 100L^{-1} at 1353 m for $^{224}\text{Ra}_{\text{ex}}$
392 and $^{223}\text{Ra}_{\text{ex}}$, respectively. Note that both activities slightly decrease after these maxima near bottom
393 depths. A similar vertical distribution is observed at station 15, where higher activities are found
394 below 1200 m. $^{223}\text{Ra}_{\text{ex}}$ activities reach values of 7.05 dpm 100L^{-1} and are higher than the $^{224}\text{Ra}_{\text{ex}}$
395 activities (maximum activity of 0.98 dpm 100L^{-1}) around 1700 m. Short-lived isotopes were even
396 measurable on small volume samples ($10.9 - 21.2$ L filtered through Mn-fibers), which is
397 uncommon for open ocean waters (Fig.5 and Table 1). Note that the activities of short-lived Ra
398 isotopes determined on Mn-fibers (small volumes) are similar to the activities determined on Mn-
399 cartridges (large volumes), but the uncertainties are much higher on Mn-fibers (Table 1). The Ra
400 activities variability between the two sampling methods may be due to cast-to-cast variability in
401 the plume height, as it was shown in the Mid Atlantic Ridge (Rudnicki et al., 1994) or to the lower
402 sampling resolution of the pump casts. The ^{227}Ac activities determined at stations 14 and 15 are
403 reported in Table 2. The ^{227}Ac activities at station 14 appear to be variable (Fig. 6), with lower
404 activities (~ 0.020 dpm 100L^{-1}) at the surface, 900 m and 1160 m and relative highest activities (\sim

405 0.035 dpm 100L⁻¹) at 1000 m, 1200 m and 1260 m. For station 15, ²²⁷Ac activities are in the range
 406 of 0.018-0.054 dpm 100L⁻¹, slightly increasing with depth.



407

408 **Figure 5.** ²²³Ra_{ex} and ²²⁴Ra_{ex} activities are shown as black circles and black triangles, respectively.
 409 Filled symbols represent activities determined by combining the activities determined using Mn-
 410 fibers and Mn-cartridges, while open symbols represent activities determined in the Mn-fibers.
 411 The graph in the right panel in grey shows, as a comparison, the vertical profiles observed off
 412 Kerguelen islands with grey triangle as ²²⁴Ra_{ex} and grey dots as ²²³Ra_{ex} (Sanial et al., 2015). Errors
 413 bars are reported but are often within the symbol. The horizontal lines represent the depth of the
 414 seafloor.

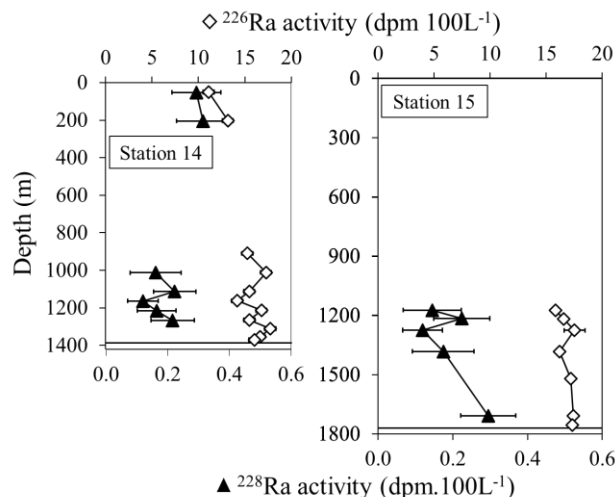


415

416 **Figure 6.** ²²⁷Ac activities are shown as black circles. The horizontal lines represent the depth of
 417 the seafloor.

418 The vertical profiles of ²²⁶Ra and ²²⁸Ra are shown in Fig. 7. ²²⁸Ra activities are up to 0.31
 419 dpm 100L⁻¹ in surface waters at station 14 but are below the detection limit at intermediate depths
 420 (700 m and 900 m at stations 14 and 15, respectively). Deeper, ²²⁸Ra activities become detectable
 421 again, increasing with depth compared to intermediate waters and reach values of 0.25 dpm 100L⁻¹
 422 near the seafloor at both stations. ²²⁶Ra activities range from 11.1 dpm 100L⁻¹ in surface waters

423 at station 14 to activities superior to 17 dpm 100L⁻¹ in the deep waters of station 15. Note that the
 424 ²²⁶Ra activities in deep waters (below 1200 m) appear to be more variable at station 14.



425

426 **Figure 7.** ²²⁶Ra and ²²⁸Ra activities are shown as white diamonds and black triangles, respectively.
 427 The horizontal lines represent the depth of the seafloor. Errors bars for ²²⁶Ra are reported but are
 428 often within the symbol.

429 4 Discussion

430 4.1 Ra isotopes and ²²⁷Ac activities above the SWIR

431 Far from any continental source, the activities of the short-lived radium isotopes rapidly
 432 decrease due to radioactive decay and mixing. The ²²³Ra and ²²⁴Ra activities in the open ocean are
 433 therefore often negligible, with the exception of waters located near the seafloor that are slightly
 434 enriched in ²²³Ra and ²²⁴Ra, as a consequence of Ra diffusion from deep-sea sediments
 435 (GEOTRACES Intermediate Data Product Group, 2021). The ²²³Ra_{ex} and ²²⁴Ra_{ex} activities
 436 reported near the seafloor at stations 14 and 15 display maximum values of 7.05 dpm 100L⁻¹ and
 437 0.98 dpm 100L⁻¹, respectively. These activities clearly exceed the activities usually found in open
 438 ocean waters (GEOTRACES Intermediate Data Product Group, 2021). As a comparison, we report
 439 in Fig. 5 all the vertical profiles of ²²³Ra_{ex} and ²²⁴Ra_{ex} determined off Kerguelen Islands in the
 440 Southern Ocean (Sanial et al., 2015). Although the waters offshore Kerguelen are slightly impacted
 441 by the islands and at depth by the input from the sediments, the ²²³Ra_{ex} and ²²⁴Ra_{ex} never exceed
 442 0.3 dpm 100L⁻¹ for both isotopes. At both stations 14 and 15, the ²²³Ra_{ex} and ²²⁴Ra_{ex} activities are
 443 very low above 900 m in agreement with the general pattern described above. At station 14, the
 444 highest ²²³Ra_{ex} and ²²⁴Ra_{ex} activities are observed at 1350 m depth, about 35 m above the seafloor
 445 while at station 15, the maximum ²²³Ra_{ex} activity is observed at 1700 m depth, about 60 m above
 446 the seafloor. As a comparison, Charette et al. (2015) reported maximum activities of 0.97 dpm
 447 100L⁻¹ for ²²³Ra_{ex} while never exceeding 0.16 dpm 100L⁻¹ for ²²⁴Ra_{ex}, in the deepest samples
 448 located ~ 80 m above the ridge crest in the TAG neutrally buoyant plume in the Mid-Atlantic
 449 Ridge. Note that all these latter activities are considerably lower than those reported here. As
 450 another comparison, Neuholz et al (2020a) reported ²²³Ra_{ex} activities up to 0.11 dpm 100L⁻¹ and
 451 up to 1.4 dpm 100L⁻¹ for ²²⁴Ra_{ex} in the Kermadec arc. The especially high ²²³Ra_{ex} and ²²⁴Ra_{ex}

452 activities reported near the seafloor at these two stations cannot be explained by diffusion from
453 bottom sediments. Considering the rocks observed in the area (e.g., lava pillows) by Humler et al.
454 (2001) and the geomorphological features (volcano shape) detected during the bathymetry survey
455 (Fig. 1), volcanism could be invoked as a source term. However, the different surveys conducted
456 in the area (Humler et al., 2001; Sato et al., 2013; this study) did not find any evidence for *active*
457 volcanism in the area. Hydrothermal activity (circulation of fluid into the basalts) is the most likely
458 candidate to explain the Ra signature reported here.

459 In contrast, the ^{227}Ac activities, up to $0.055 \text{ dpm } 100\text{L}^{-1}$, are close to the ^{227}Ac usually
460 observed in open ocean waters outside the influence of hydrothermal vents. A similar pattern was
461 observed in other studies conducted in the vicinity of low temperature ridges, where large increases
462 in $^{223}\text{Ra}_{\text{ex}}$ and $^{224}\text{Ra}_{\text{ex}}$ activities were not accompanied by an increase in ^{227}Ac activities (Moore et
463 al., 2008; Geibert et al., 2008). As a comparison, Moore et al. (2008) reported in the Puna ridge
464 activities up to $1.9 \text{ dpm } 100\text{L}^{-1}$ for $^{223}\text{Ra}_{\text{ex}}$, and up to $0.4 \text{ dpm } 100\text{L}^{-1}$ for $^{224}\text{Ra}_{\text{ex}}$ while the ^{227}Ac
465 activities never exceeded $0.02 \text{ dpm } 100\text{L}^{-1}$ (Geibert et al., 2008). This is in contrast with Kipp et
466 al. (2015) who reported significant enrichment of ^{227}Ac within the neutrally buoyant hydrothermal
467 plume overlying the TAG vent field.

468 The ^{226}Ra activities reported here are in the typical range of activities usually observed in
469 Southern Ocean waters (i.e. $15 \text{ to } 17.7 \text{ dpm } 100\text{L}^{-1}$) (Charette et al., 2007; Chung, 1987; Ku and
470 Lin, 1976; van Beek et al., 2008). However, while typical open ocean profiles display a smooth
471 increase in the ^{226}Ra activities with increasing depth (Charette et al., 2007; Chung, 1987; Ku and
472 Lin, 1976; van Beek et al., 2008), we observe a significant variability in the ^{226}Ra activities (Fig.
473 7). This is especially true at station 14 between 910 m and the bottom and to a lesser extent at
474 station 15 where a small peak is found at 1275 m. These patterns may be related to the presence of
475 a nearby hydrothermal activity, although ^{226}Ra may not be as strongly conclusive as the short-lived
476 Ra isotopes. It cannot be excluded that the high ambient ^{226}Ra activities of the Southern Ocean
477 waters would prevent any excess ^{226}Ra supplied from the ridge to be discerned.

478 In contrast to ^{226}Ra , the ^{228}Ra activities in the Southern Ocean are extremely low ($< 0.15 \text{ dpm}$
479 100L^{-1} ; van Beek et al., 2008; Sanial et al., 2015; Inoue et al., 2022) and are therefore more
480 sensitive to an input from any source term. This is often the case in surface waters in the vicinity
481 of continents/islands and near the seafloor where slight increases are detected (Charette et al.,
482 2007; van Beek et al., 2008; Sanial et al., 2014). The mid water column is often depleted in ^{228}Ra
483 relative to surface and deep waters due to slow downward and upward vertical mixing for these
484 two sources (Charette et al., 2007). At both stations 14 and 15, the ^{228}Ra activities clearly increase
485 with depth from below the detection limit (700-900 m) to ca. $0.2\text{-}0.3 \text{ dpm } 100 \text{ L}^{-1}$ near bottom
486 sediments. Such activities, however, are still in the range of activities reported in the Southern
487 Ocean near bottom sediments (see e.g., van Beek et al., 2008; Sanial et al., 2015).

488 In summary, there is a clear unusually high signature of short-lived Ra isotopes near the
489 seafloor, with the $^{223}\text{Ra}_{\text{ex}}$ activities (up to $7.05 \text{ dpm } 100 \text{ L}^{-1}$) being higher than the $^{224}\text{Ra}_{\text{ex}}$ activities
490 (up to $0.98 \text{ dpm } 100 \text{ L}^{-1}$). The patterns of ^{226}Ra , ^{228}Ra and ^{227}Ac activities are less conclusive. We
491 will thus investigate in the following sections the different processes that could lead to the patterns
492 observed among the different isotopes determined in the vicinity of a hydrothermal source.

493

494 4.2 Processes at play in the vicinity of the hydrothermal vents as indicated by
 495 $^{224}\text{Ra}_{\text{ex}}/^{228}\text{Ra}$, $^{223}\text{Ra}_{\text{ex}}/^{226}\text{Ra}$ and $^{224}\text{Ra}_{\text{ex}}/^{223}\text{Ra}$ ratios

496 Owing to the different half-lives of the Ra isotopes, the fluid circulating in the crust may
 497 not be similarly enriched in all Ra isotopes. Due to their shorter half-lives, ^{223}Ra and ^{224}Ra are
 498 regenerated faster than ^{226}Ra and ^{228}Ra (Charette et al., 2007; Garcia-Orellana et al., 2021; Fig. 8).
 499 Because circulation of seawater through the crust occurs generally over relatively short time scales,
 500 from days to a few years (Kadko and Moore, 1988; Kadko et al., 2007), Ra may be frequently
 501 flushed from the system. As the production of Ra isotopes is notably governed by their half-lives,
 502 the residence time of seawater within the crust may not allow a significant ingrowth of the long-
 503 lived Ra isotopes by radioactive decay of their parents. Thus, unless the main input process is due
 504 to weathering and dissolution of radium rich phases (Hammond et al., 1988), the circulated fluid
 505 is expected to display $^{223}\text{Ra}_{\text{ex}}/^{226}\text{Ra}$ and $^{224}\text{Ra}_{\text{ex}}/^{228}\text{Ra}$ activity ratios higher than the rock ratio. The
 506 $^{224}\text{Ra}_{\text{ex}}/^{228}\text{Ra}$ activity ratios can also be affected by the residence time of seawater into the crust
 507 depending on the type of the hydrothermal vent. Neuholz et al. (2020a) suggest that the fluid
 508 migration is relatively slow for diffuse fluids (as in ultramafic systems) and likely faster for
 509 focused venting fluids (as in volcanic systems). Similarly, Kipp et al. (2018) have observed that
 510 the $^{224}\text{Ra}_{\text{ex}}/^{228}\text{Ra}$ activity ratio is generally close to 1 in high temperature fluids, suggesting that the
 511 residence time of fluids in the crust is long enough (on the order of years) to allow these isotopes
 512 to reach secular equilibrium. In contrast, they observe $^{224}\text{Ra}_{\text{ex}}/^{228}\text{Ra}$ activity ratio often higher (up
 513 to 5.5) in low temperature hydrothermal fluids. Several processes discussed by Kipp et al. (2018)
 514 may explain the $^{224}\text{Ra}_{\text{ex}}/^{228}\text{Ra}$ activity ratios >1 . One of them is the faster regeneration of short-
 515 lived Ra isotopes compared to long-lived Ra isotopes, as explained above. The $^{224}\text{Ra}_{\text{ex}}/^{228}\text{Ra}$
 516 activity ratios can also be affected by the residence time of seawater into the crust depending on
 517 the type of the hydrothermal vent. Neuholz et al. (2020a) suggest that the fluid migration is
 518 relatively slow for diffuse fluids (as in ultramafic systems) and likely a faster for on focused
 519 venting fluids (as in volcanic systems). Alternatively, there may be a greater sorption of ^{228}Th at
 520 the end of the flow path, with the result that the circulating fluid would become enriched in ^{224}Ra .
 521 This hypothesis seems unlikely due to the high particle affinity of ^{228}Th . Finally, significant
 522 sorption or precipitation of long-lived Ra isotopes - including via BaSO_4 co-precipitation - and
 523 efficient ^{224}Ra recoil would also increase the $^{224}\text{Ra}_{\text{ex}}/^{228}\text{Ra}$ ratio in the fluid. Because the sorption
 524 process is slow compared to the decay of ^{223}Ra and ^{224}Ra , it is unlikely that short-lived Ra isotopes
 525 would be removed by sorption before decay. The $^{224}\text{Ra}_{\text{ex}}/^{228}\text{Ra}$ and $^{223}\text{Ra}_{\text{ex}}/^{226}\text{Ra}$ ratios will also
 526 decrease when the plume is transported away from the source, because radioactive decay of ^{224}Ra
 527 and ^{223}Ra is faster than ^{228}Ra and ^{226}Ra . Therefore, the $^{224}\text{Ra}_{\text{ex}}/^{228}\text{Ra}$ ratio in the plume may be
 528 indicative of the residence time of the fluid in the crust, which may be related to the fluid
 529 temperature and/or the age of the plume.

530

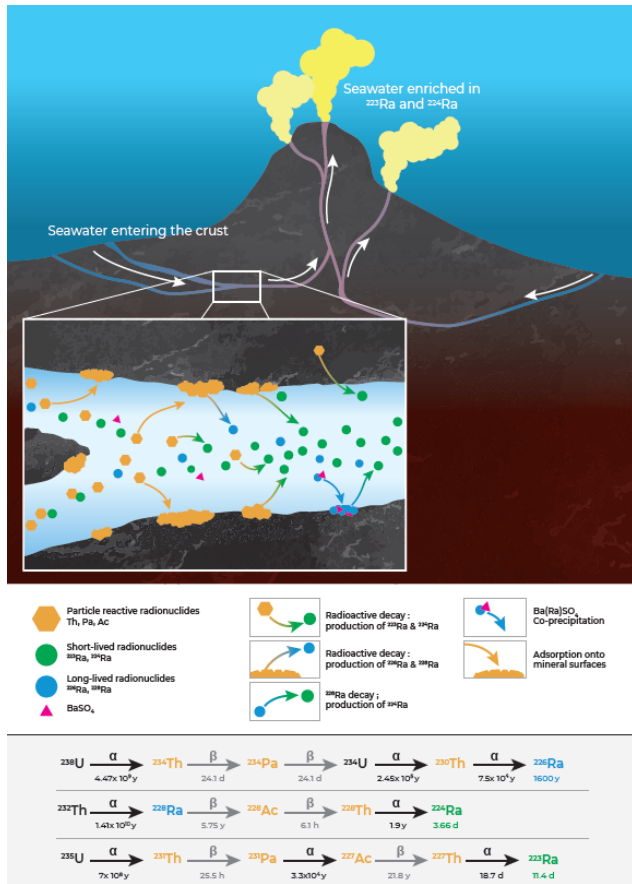
531

532 Assuming that stations 14 and 15 are located in the near vicinity of the vents, the
 533 $^{224}\text{Ra}_{\text{ex}}/^{228}\text{Ra}$ and $^{223}\text{Ra}_{\text{ex}}/^{226}\text{Ra}$ ratios may be compared to the ratios reported in hydrothermal fluids
 534 (Kipp et al., 2018), keeping in mind that these ratios decrease with increasing distance from the
 535 source. In samples displaying the highest $^{223}\text{Ra}_{\text{ex}}$ and $^{224}\text{Ra}_{\text{ex}}$ activities, we observe $^{224}\text{Ra}_{\text{ex}}/^{228}\text{Ra}$
 536 activity ratios of 3.46 at 1690 m (station 15), 1.32 at 1250 m (station 14) and 1.10 at 1200 m
 537 (station 14). An explanation that would reconcile these different ratios would be that i) the high
 538 ratio observed at station 15 may be indicative of a plume resulting from a low temperature fluid

539 (such type of fluid exhibiting ratios up to 5.5; Kipp et al., 2018) and ii) the slightly lower ratios
540 reported at station 14 may thus result from the decrease of the $^{224}\text{Ra}_{\text{ex}}/^{228}\text{Ra}$ ratio when being
541 transported away from the source. This does not mean that both stations are under the influence of
542 the same source. There could be multiple sites of hydrothermal discharge in the region.
543

544 The distinction between low and high temperature fluids is not as clear when looking at
545 the $^{223}\text{Ra}_{\text{ex}}/^{226}\text{Ra}$ activity ratios. In the data reported here, a $^{223}\text{Ra}_{\text{ex}}/^{226}\text{Ra}$ activity ratio up to 0.16
546 is observed in the deep water at station 14 and up to 0.3 in the deep water at station 15. This latter
547 value is comparable to data observed at Baby Bare Seamount and is significantly higher (about
548 one order of magnitude) than values usually observed in other vent fluids (i.e., 0.044-0.073; Kipp
549 et al., 2018). The ^{223}Ra enrichment of the circulating fluid may be explained by the particle reactive
550 behavior of Ac - compared with Ra - that will adsorb onto mineral surfaces (Moore et al., 2008;
551 Kipp et al., 2015). With time, ^{223}Ra will be produced by the decay of ^{227}Ac and will partition into
552 the aqueous phase. The seawater entering into the ridge also contains ^{232}Th , the parent of ^{224}Ra ,
553 that is deposited onto the surfaces, but in much lower concentrations than ^{231}Pa , the parent nuclide
554 of ^{227}Ac and ^{223}Ra (Fig. 8). The expected activity ratio of dissolved $^{232}\text{Th}/^{231}\text{Pa}$ in Southern Ocean
555 waters is on the order of 0.2-0.3 (calculated from Chase et al., 2003 and Thomas et al., 2006). The
556 production of ^{224}Ra is thus relatively low compared to ^{223}Ra production. This may also explain the

557 low $^{224}\text{Ra}_{\text{ex}}/^{223}\text{Ra}_{\text{ex}}$ ratios observed above the SWIR. Similar phenomena have been observed in
 558 low temperature hydrothermal vents (Moore et al., 2008; Kipp et al., 2015).



560 **Figure 8.** Conceptual figure illustrating the circulation of the fluid within a hydrothermal system
 561 and the associated partitioning of radionuclides from the U-Th decay chain.

562 4.3. Determination of vertical mixing using Ra isotopes

563 The vertical profiles of Ra isotopes can be used to estimate a vertical eddy diffusivity
 564 coefficient (K_z) (Li et al., 1980; Moore, 1972; Sarmiento et al., 1982; Ku and Luo, 1994; Charette
 565 et al., 2007; van Beek et al., 2008). The short half-lives of ^{223}Ra and ^{224}Ra probably make them
 566 less sensitive to lateral advection than other radionuclides (e.g., ^{227}Ac , ^{228}Ra and ^{226}Ra) which
 567 display longer half-lives. Moreover, the vertical profiles of ^{227}Ac , ^{228}Ra and ^{226}Ra may be more
 568 inclined to be impacted by other sources due to their longer half-life. Assuming (1) steady state on
 569 the time scale of ^{223}Ra and ^{224}Ra half-lives (i.e., the supply of ^{223}Ra and ^{224}Ra balances Ra loss by
 570 radioactive decay and mixing), (2) no addition or loss of Ra except for radioactive decay and (3)
 571 that the vertical dispersion of radium can be approximated to a diffusive process (rather than
 572 advective), then a 1D model can be written as follows:

573

574
$$\frac{dA}{dt} = K_z \frac{\partial}{\partial z} \left(\frac{\partial A}{\partial z} \right) - \lambda A = 0 \quad (1)$$

575

576 , where K_Z is the vertical eddy diffusivity coefficient, A is the Ra activity, z is the depth above
 577 the bottom and λ is the Ra decay constant. The use of a 1D model can be further justified by the
 578 structure of horizontal currents below 1000 m (Section 3.1), which are not only small, but more
 579 importantly fairly constant with depth (i.e., barotropic).

580 The solution of the equation (1) is given by:

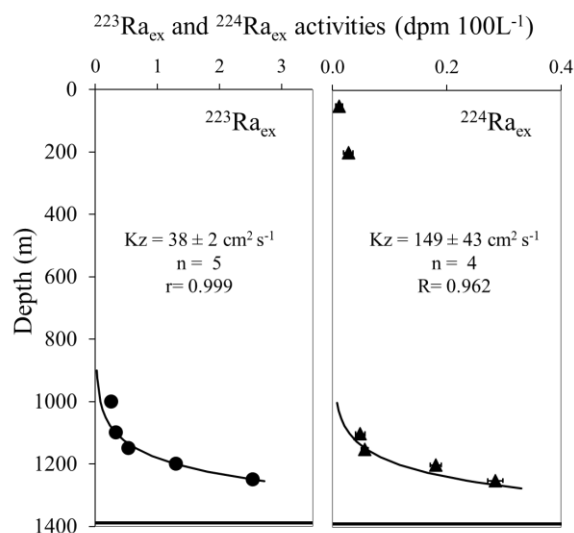
$$581 \quad A_z = A_0 \times \exp\left(-z \times \sqrt{\frac{\lambda}{K_Z}}\right) \quad (2)$$

582 , where $A=A_0$ at $z=0$ (bottom depth) and $A=0$ at $z \rightarrow \infty$. We applied the equation 2 to the vertical
 583 profiles of $^{223}\text{Ra}_{\text{ex}}$ and $^{224}\text{Ra}_{\text{ex}}$ obtained on Mn-cartridges at station 14 between 1000 m and 1250
 584 m. K_Z can be calculated from the best exponential fit coefficient of a plot of $^{223}\text{Ra}_{\text{ex}}$ or $^{224}\text{Ra}_{\text{ex}}$ vs
 585 distance from bottom, by determining the coefficient $m = (\lambda/K_Z)^{-2}$. We have chosen here not to
 586 include the activities of short-lived Ra isotopes determined on Mn-fibers in the K_Z calculation due
 587 to their large associated error bars.

588
 589 Fig. 9 shows the fit of the model to the $^{223}\text{Ra}_{\text{ex}}$ and $^{224}\text{Ra}_{\text{ex}}$ vertical profiles. We obtain K_Z of
 590 $38 \pm 2 \text{ cm}^2 \text{ s}^{-1}$ ($m = -0.01365 \pm 0.00045$; $r = 0.999$; $n = 5$) derived from $^{223}\text{Ra}_{\text{ex}}$ and $149 \pm 43 \text{ cm}^2$
 591 s^{-1} ($m = -0.01213 \pm 0.00249$; $r = 0.962$; $n = 4$) derived from $^{224}\text{Ra}_{\text{ex}}$. These K_Z values are higher
 592 than those previously reported on the Crozet or Kerguelen shelves by Charette et al. (2007) and
 593 van Beek et al. (2008), respectively ($K_Z = 1.5 \text{ cm}^2 \text{ s}^{-1}$ in both shelves at similar depths), and two
 594 or three orders of magnitude higher than the K_Z estimated by Law et al. (2003) in the open Southern
 595 Ocean ($K_Z = 0.11 \pm 0.2 \text{ cm}^2 \text{ s}^{-1}$). However, in general, rough topography at oceanic ridges leads to
 596 strong mixing compared to the ocean interior (Walter et al. 2010). For example, over the SWIR,
 597 MacKinnon et al. (2008) reported K_Z higher than $100 \text{ cm}^2 \text{ s}^{-1}$ near the seafloor in Atlantis II Frac-
 598 ture zone. High diffusivity coefficients are also observed in the vicinity of hydrothermal systems.
 599 Neuholz et al. (2020a) thus estimated K_Z of $2000 \text{ cm}^2 \text{ s}^{-1}$ in the rise height of a plume in the Ker-
 600 madec arc, while diffusivity coefficients of 130 and $300 \text{ cm}^2 \text{ s}^{-1}$ were observed at Rainbow and
 601 Lucky Strike sites (Thurnherr et al., 2022; St Laurent and Thurnherr, 2007). As another compari-
 602 son, vertical diffusivity coefficients between 40 and $800 \text{ cm}^2 \text{ s}^{-1}$ were estimated in the Mid-Atlantic
 603 Ridge region (Keir et al., 2008; Walter et al., 2010). The relatively high K_Z values reported here
 604 highlight the strong vertical mixing on the ridge flank region. Interestingly, Walter et al. (2010)
 605 suggests that slow spreading ridges, because they are characterized by a steeper, more rugged ba-
 606 thymetry, favor an enhanced level of internal wave generation from currents interacting with the
 607 topography influencing the strength of the mixing of the plume.

608
 609 Nevertheless, here we observe a significant difference between the K_Z values determined
 610 using the two different Ra isotopes, with $K_Z (^{224}\text{Ra}) > K_Z (^{223}\text{Ra})$. This trend has been invariably
 611 observed in studies reporting estimates of horizontal or vertical diffusivity coefficients (Moore,
 612 2000a; Hancock et al., 2006; Charette et al., 2007; Colbert and Hammond, 2007; Lamontagne et
 613 al., 2008; Moore and de Oliveira, 2008; Koch-Larrouy et al., 2015) and several hypotheses have
 614 been proposed to explain this difference. First, the K_Z calculation is based on the assumption that
 615 it is constant over the distance studied, although it may vary within the water column. Second, the
 616 K_Z values are derived from two isotopes displaying different half-lives. The K_Z thus obtained re-
 617 flects an integrated pattern related to the residence time of the radionuclide in the water column.
 618 The lower K_Z estimates derived from $^{223}\text{Ra}_{\text{ex}}$ may thus be explained by a longer-term integration
 619 of the signal (space, time) compared to the K_Z estimated from $^{224}\text{Ra}_{\text{ex}}$ vertical profiles. In addition,
 620 short fluctuations in end-member concentrations or water column residence time over short periods

621 of time may impact these calculations, especially for $^{224}\text{Ra}_{\text{ex}}$. Finally, Stachelhaus and Moran
 622 (2012) suggest that this difference could be attributed to differential or scale-dependent diffusion.
 623 In the present study, we thus have no reason to choose one K_Z value over the other (i.e., derived
 624 from $^{223}\text{Ra}_{\text{ex}}$ or from $^{224}\text{Ra}_{\text{ex}}$).



625

626 **Figure 9.** Vertical eddy diffusivity coefficient (K_Z) estimation at station 14 using a simple one-
 627 dimensional diffusion model applied to the vertical profiles of $^{223}\text{Ra}_{\text{ex}}$ (left panel) and $^{224}\text{Ra}_{\text{ex}}$ (right
 628 panel). The best exponential fits considering Ra data in the 1000–1250 m depth interval together
 629 with the R value are reported. The horizontal lines represent the depth of the seafloor. The
 630 uncertainties on the K_Z are derived from the uncertainty on the best exponential fit coefficient of
 631 Ra activities as function of distance from bottom (Equation 2).

632 4.4 Vertical flux of dissolved Fe in the water column

633 Very few studies reported quantification of chemical fluxes - including dissolved Fe -
 634 associated with hydrothermal vents. Recently, Neuholz et al. (2020b) quantified the Fe and Mn
 635 fluxes associated with submarine hydrothermal discharge (so called, SHD) at Brother volcano in
 636 the southern Kermadec arc (Pacific Ocean) based on the approach developed to quantify chemical
 637 fluxes associated with submarine groundwater discharge (SGD). This method is based on building
 638 the Ra inventory in the plume and requires knowledge of the volume and residence time of the
 639 plume, as well as the chemical concentrations in the fluid (endmember), including Ra and chemical
 640 concentrations. This latter information can only be obtained when a full study is conducted,
 641 presumably at a site where the presence and location of hydrothermal vents have been already
 642 identified by previous studies. Since the present study was an exploratory study, we do not have
 643 the detailed view on the volume of the plume and on the endmember concentrations, as is required
 644 by the method of Neuholz et al. (2020b). Here, we attempt to provide an estimate of the dFe flux
 645 by using a method that was applied to quantify the vertical chemical fluxes in open ocean waters
 646 that are not impacted by hydrothermal vents. The method combines the vertical eddy diffusivity
 647 coefficients K_Z estimated from the vertical profiles of Ra isotopes with the vertical gradient of dFe.
 648 Charette et al., (2007) and van Beek et al. (2008) thus quantified the vertical fluxes of dFe
 649 associated with the Crozet and Kerguelen deep-sea sediments. We used the same method using the

650 K_Z values determined from the $^{223}\text{Ra}_{\text{ex}}$ and $^{224}\text{Ra}_{\text{ex}}$ vertical profiles and the vertical gradient of dFe
 651 (data from Baudet et al., submitted). As no dFe was sampled at station 15, the flux of dFe was only
 652 determined at station 14. The vertical gradient of dFe was found to be $4.28 \cdot 10^{-4} \pm 0.236 \cdot 10^{-4} \text{ nmol}$
 653 $\text{L}^{-1} \text{ m}^{-1}$ ($r = 0.44$; $n = 16$). The sharp peak of dFe at 1300 m was not considered in the calculation
 654 (flagged as an outlier by Baudet et al., submitted). By multiplying the K_Z values by the dFe gradient
 655 between 975 m and 1364 m depth, the vertical fluxes of dFe thus obtained are $139 \pm 77 \text{ nmol m}^{-2}$
 656 d^{-1} and $552 \pm 344 \text{ nmol m}^{-2} \text{ d}^{-1}$, considering the K_Z values determined from $^{223}\text{Ra}_{\text{ex}}$ and $^{224}\text{Ra}_{\text{ex}}$,
 657 respectively. Errors on the dFe fluxes results from the propagation of the uncertainties associated
 658 with the K_Z and the vertical gradient of dFe. This flux is even higher if we consider a larger depth
 659 interval (between 700 m and the bottom) to calculate the dFe vertical gradient. A value of $9.11 \cdot 10^{-4}$
 660 $\pm 0.107 \cdot 10^{-4} \text{ nmol L}^{-1} \text{ m}^{-1}$ ($r = 0.90$; $n = 19$) is then obtained for the dFe gradient, which is slightly
 661 higher than the value calculated above. The resulting vertical flux of dFe is thus $297 \pm 38 \text{ nmol m}^{-2}$
 662 d^{-1} considering the K_Z derived from $^{223}\text{Ra}_{\text{ex}}$ and $1173 \pm 367 \text{ nmol m}^{-2} \text{ d}^{-1}$, considering the K_Z
 663 derived from $^{224}\text{Ra}_{\text{ex}}$. Overall, the dFe vertical fluxes calculated here range from 139 to 297 nmol
 664 $\text{m}^{-2} \text{ d}^{-1}$ as derived from $^{223}\text{Ra}_{\text{ex}}$ and from 552 to 1173 $\text{nmol m}^{-2} \text{ d}^{-1}$ as derived from $^{224}\text{Ra}_{\text{ex}}$.

665 Schine et al. (2021) estimated dFe fluxes of possible hydrothermal origin ranging from 440
 666 up to 530 $\text{nmol m}^{-2} \text{ d}^{-1}$ in the Pacific Southern Ocean, which is consistent with our estimates. Other
 667 studies reported dFe fluxes associated with similar systems, with, however, different units which
 668 complicates the comparison with our estimates. Neuholz et al. (2020) thus estimated dFe fluxes in
 669 the Brothers volcanoes ranging from 0.15 mol s^{-1} to 71.2 mol s^{-1} while other studies in Juan de
 670 Fuca, Rainbow vent field or again Northern Mariana Islands, reported dFe fluxes of 0.61 mol s^{-1} ,
 671 9.6 mol s^{-1} and 0.14 mol s^{-1} , respectively (German et al., 2010; Massoth et al., 1994; Buck et al.,
 672 2018). Using a geochemical model, Resing et al. (2015), estimated a global hydrothermal Fe flux
 673 of $4 \pm 1 \text{ Gmol yr}^{-1}$ while Roshan et al. (2020) estimated a much lower Fe flux of about 0.12 ± 0.07
 674 Gmol yr^{-1} taking into account particulate-dissolved Fe exchange. The dFe fluxes estimated in this
 675 study are much higher than those previously observed on the Kerguelen Plateau outside any
 676 influence of a hydrothermal activity by van Beek et al. (2008) using ^{228}Ra data ($1.0\text{-}14.3 \text{ nmol m}^{-2}$
 677 d^{-1}), by Blain et al. (2007) ($31 \text{ nmol m}^{-2} \text{ d}^{-1}$), or again by Tagliabue et al. (2014) where the authors
 678 estimate a vertical diffusive dFe flux range of $0.0016\text{-}0.0157 \mu\text{mol m}^{-2} \text{ d}^{-1}$ for the Southern Ocean.
 679 On the Crozet Plateau, also outside any influence of a hydrothermal activity, Charette et al. (2007)
 680 estimated a vertical dFe flux up to $61 \text{ nmol m}^{-2} \text{ d}^{-1}$, which is considerably lower than the one
 681 determined here. Finally, we note that the vertical dFe flux reported in this study is in the same
 682 order of magnitude as the horizontal ($390 \text{ nmol m}^{-2} \text{ d}^{-1}$) or atmospheric ($100 \text{ nmol m}^{-2} \text{ d}^{-1}$) fluxes
 683 estimated by Planquette et al. (2007) in the Crozet region. The results presented here confirm that
 684 hydrothermal systems are a significant source for dFe into the deep ocean. When combined to a
 685 strong vertical mixing, significant fluxes of dFe may be transported towards shallower waters. If
 686 this dFe reaches surface waters, it could stimulate phytoplankton blooms as suggested by Tagliabue
 687 et al. (2010), Ardyna et al. (2019) or Schine et al. (2021). If this study clearly highlights a high
 688 vertical flux of dFe at depth (below 700 m), it cannot be concluded here that dFe reaches the upper
 689 water column and contributes to fuel phytoplankton bloom.

690 4.5. Uncertainties around the Ra-based dFe flux estimation

691 Radium isotopes (with the exception of ^{226}Ra) are generally present in very low
 692 concentrations in the open ocean, necessitating the sampling of large volumes of seawater (several
 693 hundred liters) in order to measure these activities. The errors associated with $^{223}\text{Ra}_{\text{ex}}$ and $^{224}\text{Ra}_{\text{ex}}$

694 measurements are commonly estimated by an error propagation method (Garcia-Solsona et al.
695 2008), leading to errors of the order of 30 to 40 % (up to 53% for the measurement of $^{224}\text{Ra}_{\text{ex}}$ in
696 this study). Note that the relative low errors associated with the ^{223}Ra activities compared to others
697 studies (up to 14.5 % in this study) are due to i) the relatively high ^{223}Ra activities, ii) the large
698 volumes that we collected and iii) the repeated measurements (3 to 5 times) that allowed us to
699 reduce the uncertainty on the ^{227}Ac activity and thus on the ^{223}Ra activities determined using
700 RaDeCC (Le Roy et al., 2017; Léon et al., submitted). The uncertainty associated with the K_Z
701 value derives from the uncertainty on the m coefficient determined from the best exponential fit
702 of the ^{223}Ra and ^{224}Ra vertical profiles. The relative standard errors (RSD) associated with the K_Z
703 values are thus between 5 and 30 %, when using the vertical profiles of ^{223}Ra and ^{224}Ra ,
704 respectively. Finally, the uncertainty on the dFe flux is determined by propagating the uncertainty
705 on the K_Z (Fig. 9) and the uncertainty on the vertical dFe gradient. As the dFe gradient has RSD
706 of 12-55 % depending on the depth interval that is considered, the dFe fluxes display RSD of 13
707 to 62 %. Here, we prefer to report a range of dFe fluxes, the high and low values of the range being
708 determined using the K_Z values determined using either $^{223}\text{Ra}_{\text{ex}}$ or $^{224}\text{Ra}_{\text{ex}}$. The range of fluxes are
709 far greater than represented by the measurement inaccuracy described above.

710 In addition to the mathematical error associated with the estimate of the different
711 parameters that are described above, sources of uncertainty may also come from the assumptions
712 around these estimates (steady state assumption on the time scale of ^{223}Ra and ^{224}Ra half-lives, no
713 addition or loss of Ra except for radioactive decay and vertical dispersion of radium can be
714 approximated to a diffusive process, rather than advective). We cannot state with certainty that the
715 system is at steady state on the time scale of ^{223}Ra and ^{224}Ra half-lives. Despite their short half-
716 lives, it is possible that the source releases these isotopes variably over time. Moreover, the tidal
717 influence of the currents can also cause Ra concentrations to vary along the water column. The
718 vertical profiles of ^{223}Ra and ^{224}Ra activities may be affected by additional inputs - other than from
719 the hydrothermal activity - following the radioactive decay of dissolved or particulate ^{227}Ac or
720 ^{228}Th . This includes Ra that diffuses out of the sediment or Ra that may be released from bottom
721 nepheloid layers that would constitute an additional benthic Ra source, especially for ^{223}Ra which
722 has a longer half-life (Kipp et al., 2015, Neuholz et al. 2020a). However, no increase in turbidity
723 near the bottom was noticed, suggesting the absence of suspended particles in bottom layers. In
724 addition, the minor enrichments from the bottom of ^{227}Ac and ^{228}Th (not shown here) probably do
725 not release a significant amount of ^{223}Ra or ^{224}Ra and are considered to add minor uncertainties on
726 the $^{223}\text{Ra}_{\text{ex}}$ or $^{224}\text{Ra}_{\text{ex}}$ estimates. The high $^{223}\text{Ra}_{\text{ex}}$ and $^{224}\text{Ra}_{\text{ex}}$ activities observed at depth are thus
727 likely not significantly impacted by any other source that is presumably minor as a comparison to
728 the hydrothermal input. Alternatively, in hydrothermal plumes, Ra can potentially adsorb onto the
729 surfaces of manganese oxides or be incorporated into barite (BaSO_4) and then be partially removed
730 near the source (Moore and Reid, 1973; Reid et al., 1979), a process that may impact the Ra vertical
731 profiles. Finally, significant variability of the plume dispersion even at small space and time scales
732 (Ardyna et al., 2019) may be expected. This suggests that the values of K_Z and dFe fluxes estimated
733 here are likely to be valid only for that position at the time when the samples were taken.

734 In summary, taking into account all the uncertainties mentioned above and considering the
735 large uncertainties associated with K_Z and dFe fluxes, these vertical fluxes must be considered as
736 an approximate order of magnitude, limited in space and time. Still, this information is valuable,
737 since information on the chemical fluxes associated with these systems are scarce. The difficulties
738 to generate accurate fluxes of trace elements based on the Ra approach in hydrothermal deep-sea

739 environment has already been demonstrated by Neuholz et al. (2020a,b). For further investigations
740 in this region, a more detailed study is needed, including the study of the plume at a higher spatial
741 resolution (additional stations), which should allow us to better locate both the source and the
742 plume pathways and to better constrain the geochemical processes involved in these systems.

743 4.6. Speculation on the location of the source

744 Both the short half-lives and the high activities of $^{224}\text{Ra}_{\text{ex}}$ and $^{223}\text{Ra}_{\text{ex}}$ determined at stations
745 14 and 15 suggest that these stations are located in the near vicinity of the source term. These
746 vertical profiles, however, only provide a 1D view of the water column. By using physical data,
747 we attempt to have a more complete view of the dynamics in the region, which is important to
748 consider since the currents transport the plume away from the source. We aim to use these physical
749 data to estimate how far a signal released at the bottom may be transported away from the source
750 and potentially also to help locating the source term. The analysis of the horizontal circulation
751 below 1000 m presented in Section 3.1 indicates a substantial contribution from tidal currents, a
752 dominant signal at station 14, with a constant northeastward flow guided by the ridge
753 superimposed, larger at station 15 where it reaches $\sim 5 \text{ cm s}^{-1}$ according to the model (Fig. 4). The
754 periodic nature of tidal currents will tend to disperse the different radionuclides more efficiently if
755 these currents are spatially variable. Here the fairly isotropic and homogeneous nature of modeled
756 tidal ellipses (Fig. 4) suggests that barotropic tidal currents will predominantly displace the
757 different chemical elements around in a periodic movement, although we recognize that the tidal
758 model is too coarse to accurately account for the variability of the flow at the short spatial scales
759 of the local bathymetry. The background mean flow, on the other hand, consistently advects the
760 different radionuclides with a mean flow of 5 cm s^{-1} . A mean flow of 5 cm s^{-1} translates to 4.3 km
761 day^{-1} , that is a distance of $\sim 30 \text{ km}$ over one week, assuming that such high Ra signature can persist
762 over such time scale, which is already a high estimate. The source term(s) is(are) thus expected to
763 be within 30 km distance from these stations.

764 Note that we observe a decrease in the $^{224}\text{Ra}_{\text{ex}}/^{228}\text{Ra}$ activity ratios between the two stations at
765 a potential density of about 27.4 (corresponding to 1200 and 1250 m depth for station 14 and at
766 1160 and 1200 m depth for station 15) with activity ratio decreasing from 1.21 at station 14 to 0.19
767 at station 15. Assuming that stations 14 and 15 are impacted by the same source and considering
768 an eastward-northeastward transport (i.e., from station 14 to station 15; see section 3.1 and Figures
769 3 and 4), we thus estimate a transit time of about 10 days, yielding to a transport rate of 0.5 cm s^{-1} .
770 A mean flow of 0.5 cm s^{-1} translates to 0.4 km day^{-1} , that is a distance of $\sim 3 \text{ km}$ over one week.
771 The latter estimate determined using a reduced transport rate (0.5 cm s^{-1}) suggests that the source
772 term may be located even closer (within 3 km) to the investigated stations than when using the
773 transport rate reported above (5 cm s^{-1}).

774 A more precise determination of the source position, however, would require to know the Ra
775 activities (and activity ratios) at the source term and to have a more detailed view of the Ra

776 distribution in the region, in case the plume cannot be traced with temperature and suspended
777 particles.

778 **5 Conclusion**

779 These new investigations around the fracture above the SWIR have led to the establishment of
780 a very high-resolution bathymetric map of this area. While there was no clear signature on the
781 vertical profiles of temperature, dissolved oxygen, beam transmission or salinity, ^{223}Ra and ^{224}Ra
782 activities reported in this area highlight the presence of a hydrothermal system, likely located in
783 the near vicinity of the investigated stations due to the short half-lives of these radionuclides. The
784 high activities of $^{223}\text{Ra}_{\text{ex}}$ and $^{224}\text{Ra}_{\text{ex}}$ compared to long-lived Ra isotopes could be explained by a
785 faster regeneration rate of these isotopes during seawater circulation within the crust. Moreover,
786 we reported here among the highest $^{223}\text{Ra}_{\text{ex}}$ activities observed in the vicinity of hydrothermal
787 systems, unaccompanied by its parent, ^{227}Ac . This result suggests that ^{227}Ac is adsorbed onto
788 mineral surfaces during seawater circulation within the crust whereas $^{223}\text{Ra}_{\text{ex}}$ is likely released into
789 the dissolved phase. The high $^{224}\text{Ra}_{\text{ex}}/^{228}\text{Ra}$ ratios reported here are in favor of a low temperature
790 fluid. We estimated vertical diffusivity coefficients K_z of 38 - 149 $\text{cm}^2 \text{s}^{-1}$ using the vertical profiles
791 of $^{223}\text{Ra}_{\text{ex}}$ and $^{224}\text{Ra}_{\text{ex}}$ activities, respectively. By combining these coefficients to the vertical
792 gradient of dFe, we estimated dFe vertical fluxes of 139 - 297 $\text{nmol.m}^{-2}.\text{d}^{-1}$, as derived from $^{223}\text{Ra}_{\text{ex}}$
793 activities and of 552 - 1173 $\text{nmol.m}^{-2}.\text{d}^{-1}$, as derived from $^{224}\text{Ra}_{\text{ex}}$ activities. These estimates
794 highlight a strong vertical mixing on the flanks of the ridge that could promote a large flux of dFe
795 toward upper waters. This study confirms that short-lived radium isotopes are powerful tracers of
796 hydrothermal plumes associated with slow-rate spreading ridges and supports the importance of
797 low-expansion-rate ridges as significant sources of dFe to the deep ocean. However, a more
798 detailed study should be organized in order to better constrain the exact location of the
799 hydrothermal activity and the fate of the associate plume, to confirm the first results obtained here.

800 **Acknowledgments**

801 The authors thank the captain and the crew of the R/V Marion Dufresne for their assistance
802 during the SWINGS cruise. The authors also thank Emmanuel de Saint-Léger and Fabien Pérault,
803 Marion Lagarde, Nolwenn Lemaitre, Edwin Cotard, Frederic Planchon for their help during the
804 deployment of the *in-situ* pumps. We are grateful to Gérard Eldin, Sara Sergi, Corentin Clerc and
805 Loyd Izard for CTD data acquisition and preparation of Niskin bottles. We thank Anne Briaais,
806 Cédric Boulart, Cyrille Poncelet, Carla Scalabrin, Hervé Bisquay, Cedric Cotté and Lloyd Izard
807 for the hydrothermal survey and to Thomas Zambardi for his help at the LAFARA underground
808 laboratory. The help of Eric Greiner (Mercator Ocean International) who provided state of the art
809 GLORYS12 simulations is gratefully acknowledged. The authors also thank Sebastien Hervé for
810 his talent as a graphic facilitator and Antonin Soulié for his Python skills. The SWINGS project
811 was supported by the French Oceanographic Fleet, ANR (Agence Nationale de la Recherche ;
812 ANR) CNRS/ INSU (Centre Nationale de la Recherche Scientifique/Institut National des Sciences
813 de l'Univers) and ISblue (ANR-17-EURE-0015). This study has been partially supported through
814 the grant EUR TESS N°ANR-18-EURE-0018 in the framework of the Programme des
815 Investissements d'Avenir. The authors thank Reiner Schlitzer for the Ocean Data View software
816 (<https://odv.awi.de>, 2020) and R Pawlowicz for the M_Map Matlab toolbox. The GEOTRACES
817 2021 Intermediate Data Product (IDP 2021) represents an international collaboration and is
818 endorsed by the Scientific Committee on Oceanic Research (SCOR). M.A.C. was funded by the

819 National Science Foundation Chemical Oceanography program (OCE-1829431). The many
820 researchers and funding agencies responsible for the collection of data and quality control are
821 thanked for their contribution to the IDP2021.

822

823 **Author contributions**

824 CJ and HP wrote the proposal to secure fundings for the project and were co-PIs of the
825 SWINGS cruise. The sampling design for fieldwork was conducted by HP, CJ, PvB, VS and FV.
826 PvB, MS, ML, HP and CC mobilized equipment and consumables for fieldwork. Samples were
827 collected in the field by PvB, VS, ML, HP and CB. Sample analysis was conducted by PvB, VS,
828 ML, MS, MAC, HP and CC. FV and EK worked on the physical modeling and observation part.
829 ML, PvB and VS analyzed and interpreted the data, ML produced the figures and wrote the paper.
830 All authors provided comments on subsequent drafts of the paper.

831

832 **References**

- 833 Anderson, R.F., Bacon, M.P., Brewer, P.G., 1983. Removal of ^{230}Th and ^{231}Pa from the open
834 ocean. *Earth Planet. Sci. Lett.* 62, 7–23. [https://doi.org/10.1016/0012-821X\(83\)90067-5](https://doi.org/10.1016/0012-821X(83)90067-5)
- 835 Ardyna, M., Lacour, L., Sergi, S., d’Ovidio, F., Sallée, J.-B., Rembauville, M., Blain, S.,
836 Tagliabue, A., Schlitzer, R., Jeandel, C., Arrigo, K.R., Claustre, H., 2019. Hydrothermal vents
837 trigger massive phytoplankton blooms in the Southern Ocean. *Nat. Commun.* 10, 2451.
- 838 Baker et al., 2004, *Geochem. Geophys. Geosyst.* 5, Q08002, Hydrothermal venting in magma
839 deserts: The ultraslow-spreading Gakkel and Southwest Indian Ridges,
840 [doi:10.1029/2004GC000712](https://doi.org/10.1029/2004GC000712).
- 841 Baker, E.T., German, C.R., Elderfield, H., 2013. Hydrothermal Plumes Over Spreading-Center
842 Axes: Global Distributions and Geological Inferences, in: Humphris, S.E., Zierenberg, R.A.,
843 Mullineaux, L.S., Thomson, R.E. (Eds.), *Geophysical Monograph Series*. American Geophysical
844 Union, Washington, D. C., pp. 47–71. <https://doi.org/10.1029/GM091p0047>
- 845 Baskaran, M., Murphy, D.J., Santschi, P.H., Orr, J.C., Schink, D.R., 1993. A method for rapid in
846 situ extraction and laboratory determination of Th, Pb, and Ra isotopes from large volumes of
847 seawater. *Deep Sea Res. Part Oceanogr. Res. Pap.* 40, 849–865. [https://doi.org/10.1016/0967-](https://doi.org/10.1016/0967-0637(93)90075-E)
848 [0637\(93\)90075-E](https://doi.org/10.1016/0967-0637(93)90075-E)
- 849 Blain, S., Quéguiner, B., Armand, L., Belviso, S., Bombled, B., Bopp, L., Bowie, A., Brunet, C.,
850 Brussaard, C., Carlotti, F., Christaki, U., Corbière, A., Durand, I., Ebersbach, F., Fuda, J.-L.,
851 Garcia, N., Gerringa, L., Griffiths, B., Guigue, C., Guillerm, C., Jacquet, S., Jeandel, C., Laan,
852 P., Lefèvre, D., Lo Monaco, C., Malits, A., Mosseri, J., Obernosterer, I., Park, Y.-H., Picheral,
853 M., Pondaven, P., Remenyi, T., Sandroni, V., Sarthou, G., Savoye, N., Scouarnec, L., Souhaut,
854 M., Thuiller, D., Timmermans, K., Trull, T., Uitz, J., van Beek, P., Veldhuis, M., Vincent, D.,
855 Viollier, E., Vong, L., Wagener, T., 2007. Effect of natural iron fertilization on carbon
856 sequestration in the Southern Ocean. *Nature* 446, 1070–1074.
857 <https://doi.org/10.1038/nature05700>
- 858 Boyd, P.W., Ellwood, M.J., 2010. The biogeochemical cycle of iron in the ocean. *Nat. Geosci.* 3,
859 675–682. <https://doi.org/10.1038/ngeo964>

- 860 Buck, N.J., Resing, J.A., Baker, E.T., Lupton, J.E., 2018. Chemical Fluxes From a Recently
861 Erupted Shallow Submarine Volcano on the Mariana Arc. *Geochem. Geophys. Geosystems* 19,
862 1660–1673. <https://doi.org/10.1029/2018GC007470>
- 863 Campbell, A.C., Palmer, M.R., Klinkhammer, G.P., Bowers, T.S., Edmond, J.M., Lawrence,
864 J.R., Casey, J.F., Thompson, G., Humphris, S., Rona, P., Karson, J.A., 1988. Chemistry of hot
865 springs on the Mid-Atlantic Ridge. *Nature* 335, 514–519. <https://doi.org/10.1038/335514a0>
- 866 Charette, M.A., Gonneea, M.E., Morris, P.J., Statham, P., Fones, G., Planquette, H., Salter, I.,
867 Garabato, A.N., 2007. Radium isotopes as tracers of iron sources fueling a Southern Ocean
868 phytoplankton bloom. *Deep Sea Res. Part II Top. Stud. Oceanogr.* 54, 1989–1998.
869 <https://doi.org/10.1016/j.dsr2.2007.06.003>
- 870 Chase, Z., Anderson, R.F., Fleisher, M.Q., Kubik, P.W., 2003. Scavenging of ^{230}Th , ^{231}Pa and
871 ^{10}Be in the Southern Ocean (SW Pacific sector): the importance of particle flux, particle
872 composition and advection. *Deep Sea Res. Part II Top. Stud. Oceanogr.* 50, 739–768.
873 [https://doi.org/10.1016/S0967-0645\(02\)00593-3](https://doi.org/10.1016/S0967-0645(02)00593-3)
- 874 Chen, J., Tao, C., Liang, J., Liao, S., Dong, C., Li, H., Li, W., Wang, Y., Yue, X., He, Y., 2018.
875 Newly discovered hydrothermal fields along the ultraslow-spreading Southwest Indian Ridge
876 around 63°E . *Acta Oceanol. Sin.* 37, 61–67. <https://doi.org/10.1007/s13131-018-1333-y>
- 877 Chung, Y., 1987. ^{226}Ra in the western Indian Ocean. *Earth Planet. Sci. Lett.* 85, 11–27.
878 [https://doi.org/10.1016/0012-821X\(87\)90017-3](https://doi.org/10.1016/0012-821X(87)90017-3)
- 879 Cochran, J.K., 1982. The oceanic chemistry of the U- and Th-series nuclides.
- 880 Colbert, S.L., Hammond, D.E., 2007. Temporal and spatial variability of radium in the coastal
881 ocean and its impact on computation of nearshore cross-shelf mixing rates. *Cont. Shelf Res.* 27,
882 1477–1500. <https://doi.org/10.1016/j.csr.2007.01.003>
- 883 Corliss, J.B., Dymond, J., Gordon, L.I., Edmond, J.M., Von Herzen, R.P., Ballard, R.D., Green,
884 K., Williams, D., Bainbridge, A., Crane, K., Van Andel, T.H., 1979. Submarine Thermal Springs
885 on the Galápagos Rift. *Science* 203, 1073–1083. <https://doi.org/10.1126/science.203.4385.1073>
- 886 Edmond, J.M., Measures, C., McDuff, R.E., Chan, L.H., Collier, R., Grant, B., Gordon, L.I.,
887 Corliss, J.B., 1979. Ridge crest hydrothermal activity and the balances of the major and minor
888 elements in the ocean: The Galapagos data. *Earth Planet. Sci. Lett.* 46, 1–18.
889 [https://doi.org/10.1016/0012-821X\(79\)90061-X](https://doi.org/10.1016/0012-821X(79)90061-X)
- 890 Edmond, J.M., Von Damm, K.L., McDuff, R.E., Measures, C.I., 1982. Chemistry of hot springs
891 on the East Pacific Rise and their effluent dispersal. *Nature* 297, 187–191.
892 <https://doi.org/10.1038/297187a0>
- 893 Egbert, G. D., Erofeeva, S. Y., 2002. Efficient inverse modeling of barotropic ocean tides.
894 *Journal of Atmospheric and Oceanic Technology*, 19 (2), 183 – 204. doi: 10.1175/1520-
895 0426(2002)019h0183:EIMOBOi2.0.CO;2
- 896 Elderfield, H., Schultz, A., 1996. Mid-Ocean Ridge Hydrothermal Fluxes and the Chemical
897 Composition of the Ocean. *Annu. Rev. Earth Planet. Sci.* 24, 191–224.
898 <https://doi.org/10.1146/annurev.earth.24.1.191>
- 899 Garcia-Orellana, J., Rodellas, V., Tamborski, J., Diego-Feliu, M., van Beek, P., Weinstein, Y.,
900 Charette, M., Alorda-Kleinglass, A., Michael, H.A., Stieglitz, T., Scholten, J., 2021. Radium
901 isotopes as submarine groundwater discharge (SGD) tracers: Review and recommendations.
902 *Earth-Sci. Rev.* 220, 103681. <https://doi.org/10.1016/j.earscirev.2021.103681>
- 903 Garcia-Solsona, E., Garcia-Orellana, J., Masqué, P., Dulaiova, H., 2008. Uncertainties associated
904 with ^{223}Ra and ^{224}Ra measurements in water via a Delayed Coincidence Counter (RaDeCC).
905 *Mar. Chem.* 22.

- 906 Geibert, W., Charette, M., Kim, G., Moore, W.S., Street, J., Young, M., Paytan, A., 2008. The
907 release of dissolved actinium to the ocean: A global comparison of different end-members. *Mar.*
908 *Chem.* 109, 409–420. <https://doi.org/10.1016/j.marchem.2007.07.005>
- 909 German, C.R., Baker, E.T., Mevel, C., Tamaki, K., The Fuji Science Team, 1998. Hydrothermal
910 activity along the southwest Indian ridge. *Nature* 395, 490–493. <https://doi.org/10.1038/26730>
- 911 German, C.R., Seyfried, W.E., 2014. Hydrothermal Processes, in: *Treatise on Geochemistry*.
912 Elsevier, pp. 191–233. <https://doi.org/10.1016/B978-0-08-095975-7.00607-0>
- 913 German, C.R., Von Damm, K.L., 2003. Hydrothermal Processes, in: *Treatise on Geochemistry*.
914 Elsevier, pp. 181–222. <https://doi.org/10.1016/B0-08-043751-6/06109-0>
- 915 German, C.R., Thurnherr, A.M., Knoery, J., Charlou, J.-L., Jean-Baptiste, P., Edmonds, H.N.,
916 2010. Heat, volume and chemical fluxes from submarine venting: A synthesis of results from the
917 Rainbow hydrothermal field, 36°N MAR. *Deep Sea Res. Part Oceanogr. Res. Pap.* 57, 518–527.
918 <https://doi.org/10.1016/j.dsr.2009.12.011>
- 919 Hammond, D.E., Zuckin, J.G., Ku, T.-L., 1988. The kinetics of radioisotope exchange between
920 brine and rock in a geothermal system. *J. Geophys. Res. Solid Earth* 93, 13175–13186.
921 <https://doi.org/10.1029/JB093iB11p13175>
- 922 Han, X., Wu, G., Cui, R., Qiu, Z., Deng, X., Wang, Y., Scientific Party Of Dy115-21 Cruise Leg
923 7, 2010. Discovery of a Hydrothermal Sulfide Deposit on the Southwest Indian Ridge at 49.2°E
924 2010, OS21C-1531.
- 925 Hancock, G.J., Webster, Ian.T., Stieglitz, T.C., 2006. Horizontal mixing of Great Barrier Reef
926 waters: Offshore diffusivity determined from radium isotope distribution. *J. Geophys. Res.* 111,
927 C12019. <https://doi.org/10.1029/2006JC003608>
- 928 Henderson, P.B., Morris, P.J., Moore, W.S.,
929 Charette, M.A., 2013. Methodological advances for measuring low-level radium isotopes in
929 seawater. *J. Radioanal. Nucl. Chem.* 296, 357–362. <https://doi.org/10.1007/s10967-012-2047-9>
- 930 HUMLER Eric, 2001. MD 121 / SWIFT cruise, Marion Dufresne R/V.
931 <https://doi.org/10.17600/1200030>
- 932 Humphris, S.E., Zierenberg, R.A., Mullineaux, L.S., Thomson, R.E. (Eds.), 1995. Seafloor
933 Hydrothermal Systems: Physical, Chemical, Biological, and Geological Interactions:
934 Humphris/Seafloor Hydrothermal Systems: Physical, Chemical, Biological, and Geological
935 Interactions, Geophysical Monograph Series. American Geophysical Union, Washington, D. C.
936 <https://doi.org/10.1029/GM091>
- 937 Inoue, M., Hanaki, S., Kameyama, H., Kumamoto, Y., Nagao, S., 2022. Unique current
938 connecting Southern and Indian Oceans identified from radium distributions. *Sci. Rep.* 12, 1781.
939 <https://doi.org/10.1038/s41598-022-05928-y>
- 940 Intermediate Data Product Group, 2021. The GEOTRACES Intermediate Data Product 2021
941 (IDP2021). <https://doi.org/10.5285/CF2D9BA9-D51D-3B7C-E053-8486ABC0F5FD>
- 942 Kadko, D., 1996. Radioisotopic studies of submarine hydrothermal vents. *Rev. Geophys.* 34,
943 349–366. <https://doi.org/10.1029/96RG01762>
- 944 Kadko, D., Butterfield, D.A., 1998. The relationship of hydrothermal fluid composition and
945 crustal residence time to maturity of vent fields on the Juan de Fuca Ridge. *Geochim.*
946 *Cosmochim. Acta* 62, 1521–1533. [https://doi.org/10.1016/S0016-7037\(98\)00088-X](https://doi.org/10.1016/S0016-7037(98)00088-X)
- 947 Kadko, D., Gronvold, K., Butterfield, D., 2007. Application of radium isotopes to determine
948 crustal residence times of hydrothermal fluids from two sites on the Reykjanes Peninsula,
949 Iceland. *Geochim. Cosmochim. Acta* 71, 6019–6029. <https://doi.org/10.1016/j.gca.2007.09.018>

- 950 Kadko, D., Moore, W., 1988. Radiochemical constraints on the crustal residence time of
951 submarine hydrothermal fluids: Endeavour Ridge. *Geochim. Cosmochim. Acta* 52, 659–668.
952 [https://doi.org/10.1016/0016-7037\(88\)90328-6](https://doi.org/10.1016/0016-7037(88)90328-6)
- 953 Keir, R.S., Schmale, O., Walter, M., Sölltenfuß, J., Seifert, R., Rhein, M., 2008. Flux and
954 dispersion of gases from the “Drachenschlund” hydrothermal vent at 8° 18' S, 13° 30' W on the
955 Mid-Atlantic Ridge. *Earth and Planetary Science Letters*, 270 (2008), pp. 338–348.
956 <https://doi.org/10.1016/j.epsl.2008.03.054>
- 957 Kipp, L.E., Charette, M.A., Hammond, D.E., Moore, W.S., 2015. Hydrothermal vents: A
958 previously unrecognized source of actinium-227 to the deep ocean. *Mar. Chem.* 177, 583–590.
959 <https://doi.org/10.1016/j.marchem.2015.09.002>
- 960 Kipp, L.E., Sanial, V., Henderson, P.B., van Beek, P., Reyss, J.-L., Hammond, D.E., Moore,
961 W.S., Charette, M.A., 2018. Radium isotopes as tracers of hydrothermal inputs and neutrally
962 buoyant plume dynamics in the deep ocean. *Mar. Chem.* 201, 51–65.
963 <https://doi.org/10.1016/j.marchem.2017.06.011>
- 964 Koch-Larrouy, A., Atmadipoera, A., van Beek, P., Madec, G., Aucan, J., Lyard, F., Grelet, J.,
965 Souhaut, M., 2015. Estimates of tidal mixing in the Indonesian archipelago from
966 multidisciplinary INDOMIX in-situ data. *Deep Sea Res. Part Oceanogr. Res. Pap.* 106, 136–153.
967 <https://doi.org/10.1016/j.dsr.2015.09.007>
- 968 Krishnaswami, S., Graustein, W.C., Turekian, K.K., Dowd, J.F., 1982. Radium, thorium, and
969 radioactive lead isotopes in ground waters: application to the in-situ determination of adsorption
970 rate constants and retardation factors. *Water Resour. Res.* 18, 1663–1675.
- 971 Ku, T.L., Li, Y.H., Mathieu, G.G., Wong, H.K., 1970. Radium in the Indian-Antarctic Ocean
972 south of Australia. *J. Geophys. Res.* 75, 5286–5292. <https://doi.org/10.1029/JC075i027p05286>
- 973 Ku, T.-L., Lin, M.-C., 1976. 226Ra distribution in the Antarctic Ocean. *Earth Planet. Sci. Lett.*
974 32, 236–248. [https://doi.org/10.1016/0012-821X\(76\)90064-9](https://doi.org/10.1016/0012-821X(76)90064-9)
- 975 Ku, T.-L., Luo, S., 1994. New appraisal of radium 226 as a large-scale oceanic mixing tracer. *J.*
976 *Geophys. Res.* 99, 10255. <https://doi.org/10.1029/94JC00089>
- 977 Lamontagne, S., Le Gal La Salle, C., Hancock, G.J., Webster, I.T., Simmons, C.T., Love, A.J.,
978 James-Smith, J., Smith, A.J., Kämpf, J., Fallowfield, H.J., 2008. Radium and radon radioisotopes
979 in regional groundwater, intertidal groundwater, and seawater in the Adelaide Coastal Waters
980 Study area: Implications for the evaluation of submarine groundwater discharge. *Mar. Chem.*
981 109, 318–336. <https://doi.org/10.1016/j.marchem.2007.08.010>
- 982 Law, C.S., Abraham, E.R., Watson, A., Liddicoat, M., 2003. Vertical eddy diffusion and nutrient
983 supply to the surface mixed layer of the Antarctic Circumpolar Current. *J. Geophys. Res.* 108,
984 3272. <https://doi.org/10.1029/2002JC001604>
- 985 Lellouche, J.-M., Greiner, E., Bourdallé-Badie, R., Garric, G., Melet, A., Drévillon, M., Bricaud
986 C., Hamon, M., Le Galloudec, O., Regnier, C., Candela, T., Testut, C.-E., Gasparin, F.,
987 Ruggiero, G., Benkiran, M., Drillet, Y., Le Traon, P.-Y. (2021). The Copernicus Global 1/12°
988 Oceanic and Sea Ice GLORYS12 Reanalysis. *Front. Earth Sci.* 9:698876. doi:
989 10.3389/feart.2021.698876
- 990 Le Roy, E., Sanial, V., Lacan, F., van Beek, P., Souhaut, M., Charette, M.A., Henderson, P.B.,
991 2019. Insight into the measurement of dissolved 227Ac in seawater using radium delayed
992 coincidence counter. *Mar. Chem.* 212, 64–73. <https://doi.org/10.1016/j.marchem.2019.04.002>
- 993 Lemaitre, N., de Souza, G.F., Archer, C., Wang, R.-M., Planquette, H., Sarthou, G., Vance, D.,
994 2020. Pervasive sources of isotopically light zinc in the North Atlantic Ocean. *Earth Planet. Sci.*
995 *Lett.* 539, 116216. <https://doi.org/10.1016/j.epsl.2020.116216>

- 996 Léon, M., Van Beek, P., Sanial, V., Souhaut, M., Henderson, P., Charette, M.A., 2024.
997 Comparison of methods to determine extraction efficiencies of Ra isotopes and ^{227}Ac from
998 large volume seawater samples. *Marine Chemistry* 258, 104328.
999 <https://doi.org/10.1016/j.marchem.2023.104328>
- 1000 Li, Y.-H., Feely, H.W., Toggweiler, J.R., 1980. ^{228}Ra and ^{228}Th concentrations in GEOSECS
1001 Atlantic surface waters. *Deep Sea Res. Part Oceanogr. Res. Pap.* 27, 545–555.
1002 [https://doi.org/10.1016/0198-0149\(80\)90039-4](https://doi.org/10.1016/0198-0149(80)90039-4)
- 1003 Liao, S., Tao, C., Li, H., Zhang, G., Liang, J., Yang, W., Wang, Y., 2018. Surface sediment
1004 geochemistry and hydrothermal activity indicators in the Dragon Horn area on the Southwest
1005 Indian Ridge. *Marine Geology* 398, 22–34. <https://doi.org/10.1016/j.margeo.2017.12.005>
- 1006 Livingston, H.D., Cochran, J.K., 1987. Determination of transuranic and thorium isotopes in
1007 ocean water: In solution and in filterable particles. *J. Radioanal. Nucl. Chem. Artic.* 115, 299–
1008 308. <https://doi.org/10.1007/BF02037445>
- 1009 Lough, A.J.M., Tagliabue, A., Demasy, C., Resing, J.A., Mellett, T., Wyatt, N.J., Lohan, M.C.,
1010 2023. Tracing differences in iron supply to the Mid-Atlantic Ridge valley between hydrothermal
1011 vent sites: implications for the addition of iron to the deep ocean. *Biogeosciences* 20, 405–420.
1012 <https://doi.org/10.5194/bg-20-405-2023>
- 1013 Mann, D.R., Casso, S.A., 1984. In situ chemisorption of radiocesium from seawater. *Mar. Chem.*
1014 14, 307–318. [https://doi.org/10.1016/0304-4203\(84\)90027-6](https://doi.org/10.1016/0304-4203(84)90027-6)
- 1015 Massoth, G.J., Baker, E.T., Lupton, J.E., Feely, R.A., Butterfield, D.A., Von Damm, K.L., Roe,
1016 K.K., Lebon, G.T., 1994. Temporal and spatial variability of hydrothermal manganese and iron
1017 at Cleft segment, Juan de Fuca Ridge. *J. Geophys. Res. Solid Earth* 99, 4905–4923.
1018 <https://doi.org/10.1029/93JB02799>
- 1019 Moore, W., 1972. Radium-228: Application to thermocline mixing studies. *Earth Planet. Sci.*
1020 *Lett.* 16, 421–422. [https://doi.org/10.1016/0012-821X\(72\)90161-6](https://doi.org/10.1016/0012-821X(72)90161-6)
- 1021 Moore, W.S., 2008. Fifteen years experience in measuring ^{224}Ra and ^{223}Ra by delayed-
1022 coincidence counting. *Mar. Chem.* 109, 188–197.
1023 <https://doi.org/10.1016/j.marchem.2007.06.015>
- 1024 Moore, W.S., 2000a. Determining coastal mixing rates using radium isotopes. *Cont. Shelf Res.*
1025 20, 1993–2007. [https://doi.org/10.1016/S0278-4343\(00\)00054-6](https://doi.org/10.1016/S0278-4343(00)00054-6)
- 1026 Moore, W.S., 2000b. Ages of continental shelf waters determined from ^{223}Ra and ^{224}Ra . *J.*
1027 *Geophys. Res.* 105, 22117–22122. <https://doi.org/10.1029/1999JC000289>
- 1028 Moore, W.S., Cai, P., 2013. Calibration of RaDeCC systems for ^{223}Ra measurements. *Mar.*
1029 *Chem.* 156, 130–137. <https://doi.org/10.1016/j.marchem.2013.03.002>
- 1030 Moore, W.S., de Oliveira, J., 2008. Determination of residence time and mixing processes of the
1031 Ubatuba, Brazil, inner shelf waters using natural Ra isotopes. *Estuar. Coast. Shelf Sci.* 76, 512–
1032 521. <https://doi.org/10.1016/j.ecss.2007.07.042>
- 1033 Moore, W.S., Frankle, J.D., Benitez-Nelson, C.R., Früh-Green, G.L., Lang, S.Q., 2021.
1034 Activities of ^{223}Ra and ^{226}Ra in Fluids From the Lost City Hydrothermal Field Require Short
1035 Fluid Residence Times. *J. Geophys. Res. Oceans* 126. <https://doi.org/10.1029/2021JC017886>
- 1036 Moore, W.S., Reid, D.F., 1973. Extraction of radium from natural waters using manganese-
1037 impregnated acrylic fibers. *J. Geophys. Res.* 78, 8880–8886.
1038 <https://doi.org/10.1029/JC078i036p08880>
- 1039 Moore, W.S., Ussler, W., Paull, C.K., 2008. Short-lived radium isotopes in the Hawaiian margin:
1040 Evidence for large fluid fluxes through the Puna Ridge. *Mar. Chem.* 109, 421–430.
1041 <https://doi.org/10.1016/j.marchem.2007.09.010>

- 1042 Neuholz, R., Schnetger, B., Kleint, C., Koschinsky, A., Lettmann, K., Sander, S., Türke, A.,
1043 Walter, M., Zitoun, R., Brumsack, H.-J., 2020a. Near-field hydrothermal plume dynamics at
1044 Brothers Volcano (Kermadec Arc): A short-lived radium isotope study. *Chem. Geol.* 533,
1045 119379. <https://doi.org/10.1016/j.chemgeo.2019.119379>
- 1046 Neuholz R, Kleint C, Schnetger B, Koschinsky A, Laan P, Middag R, Sander S, Thal J, Türke A,
1047 Walter M, Zitoun R, Brumsack H-J; 2020b Submarine Hydrothermal Discharge and Fluxes of
1048 Dissolved Fe and Mn, and He Isotopes at Brothers Volcano Based on Radium Isotopes. *Minerals*
1049 10, 969.
- 1050 Nozaki, Y., 1993. Actinium-227: A Steady State Tracer for the Deep-sea Basin-wide Circulation
1051 and Mixing Studies, in: Elsevier Oceanography Series. Elsevier, pp. 139–156.
1052 [https://doi.org/10.1016/S0422-9894\(08\)71323-0](https://doi.org/10.1016/S0422-9894(08)71323-0)
- 1053 Nozaki, Y., 1984. Excess ^{227}Ac in deep ocean water. *Nature* 310, 486–488.
1054 <https://doi.org/10.1038/310486a0>
- 1055 Park, Y.-H., Gamberoni, L., 1997. Cross-frontal exchange of Antarctic Intermediate Water and
1056 Antarctic Bottom Water in the Crozet Basin. *Deep Sea Res. Part II Top. Stud. Oceanogr.* 44,
1057 963–986. [https://doi.org/10.1016/S0967-0645\(97\)00004-0](https://doi.org/10.1016/S0967-0645(97)00004-0)
- 1058 Patriat, P., Sauter, D., Munsch, M., Parson, L., 1997. A Survey of the Southwest Indian Ridge
1059 Axis Between Atlantis II Fracture Zone and the Indian Ocean Triple Junction: Regional Setting
1060 and Large Scale Segmentation. *Mar. Geophys. Res.* 19, 457–480.
1061 <https://doi.org/10.1023/A:1004312623534>
- 1062 Ramirez-Llodra, E., Brandt, A., Danovaro, R., De Mol, B., Escobar, E., German, C.R., Levin,
1063 L.A., Martinez Arbizu, P., Menot, L., Buhl-Mortensen, P., Narayanaswamy, B.E., Smith, C.R.,
1064 Tittensor, D.P., Tyler, P.A., Vanreusel, A., Vecchione, M., 2010. Deep, diverse and definitely
1065 different: unique attributes of the world's largest ecosystem. *Biogeosciences* 7, 2851–2899.
1066 <https://doi.org/10.5194/bg-7-2851-2010>
- 1067 Resing, J.A., Sedwick, P.N., German, C.R., Jenkins, W.J., Moffett, J.W., Sohst, B.M., Tagliabue,
1068 A., 2015. Basin-scale transport of hydrothermal dissolved metals across the South Pacific Ocean.
1069 *Nature* 523, 200–203. <https://doi.org/10.1038/nature14577>
- 1070 Rudnicki, M.D., James, R.H., Elderfield, H., 1994. Near-field variability of the TAG non-
1071 buoyant plume, 26°N, Mid-Atlantic Ridge. *Earth Planet. Sci. Lett.* 127, 1–10.
1072 [https://doi.org/10.1016/0012-821X\(94\)90193-7](https://doi.org/10.1016/0012-821X(94)90193-7)
- 1073 Saito, M.A., Noble, A.E., Tagliabue, A., Goepfert, T.J., Lamborg, C.H., Jenkins, W.J., 2013.
1074 Slow-spreading submarine ridges in the South Atlantic as a significant oceanic iron source. *Nat.*
1075 *Geosci.* 6, 775–779. <https://doi.org/10.1038/ngeo1893>
- 1076 Sanial, V., van Beek, P., Lansard, B., d'Ovidio, F., Kestenare, E., Souhaut, M., Zhou, M., Blain,
1077 S., 2014. Study of the phytoplankton plume dynamics off the Crozet Islands (Southern Ocean):
1078 A geochemical-physical coupled approach. *J. Geophys. Res. Oceans* 119, 2227–2237.
1079 <https://doi.org/10.1002/2013JC009305>
- 1080 Sanial, V., van Beek, P., Lansard, B., Souhaut, M., Kestenare, E., d'Ovidio, F., Zhou, M., Blain,
1081 S., 2015. Use of Ra isotopes to deduce rapid transfer of sediment-derived inputs off Kerguelen.
1082 *Biogeosciences* 12, 1415–1430. <https://doi.org/10.5194/bg-12-1415-2015>
- 1083 Sarmiento, J.L., Rooth, C.G.H., Broecker, W.S., 1982. Radium 228 as a tracer of basin wide
1084 processes in the abyssal ocean. *J. Geophys. Res.* 87, 9694.
1085 <https://doi.org/10.1029/JC087iC12p09694>
- 1086 Sarthou, G., Vincent, D., Christaki, U., Obernosterer, I., Timmermans, K.R., Brussaard, C.P.D.,
1087 2008. The fate of biogenic iron during a phytoplankton bloom induced by natural fertilisation:

- 1088 Impact of copepod grazing. *Deep Sea Res. Part II Top. Stud. Oceanogr.* 55, 734–751.
1089 <https://doi.org/10.1016/j.dsr2.2007.12.033>
- 1090 Sato, T., Okino, K., Sato, H., Mizuno, M., Hanyu, T., Seama, N., 2013. Magmatic activities on
1091 the Southwest Indian Ridge between 35°E and 40°E, the closest segment to the Marion hotspot.
1092 *Geochemistry, Geophysics, Geosystems* 14, 5286–5307. <https://doi.org/10.1002/2013GC004814>
- 1093 Sauter, D. and Cannat, M., 2010. The ultraslow spreading Southwest Indian ridge. *Diversity of*
1094 *hydrothermal systems on slow spreading ocean ridges*, 88, pp.153-173.
- 1095 Schine, C.M.S., Alderkamp, A.-C., van Dijken, G., Gerringa, L.J.A., Sergi, S., Laan, P., van
1096 Haren, H., van de Poll, W.H., Arrigo, K.R., 2021. Massive Southern Ocean phytoplankton bloom
1097 fed by iron of possible hydrothermal origin. *Nat. Commun.* 12, 1211.
1098 <https://doi.org/10.1038/s41467-021-21339-5>
- 1099 St Laurent, L.C., Thurnherr, A.M., 2007. Intense mixing of lower thermocline water on the crest
1100 of the Mid-Atlantic Ridge. *Nature* 448, 680–683. <https://doi.org/10.1038/nature06043>
- 1101 Stachelhaus, S.L., Moran, S.B., 2012. A simple differential diffusion model to account for the
1102 discrepancy between ²²³Ra- and ²²⁴Ra-based eddy diffusivities: DIFFERENTIAL DIFFUSION
1103 AND Ra-BASED *K*. *J. Geophys. Res. Oceans* 117, n/a-n/a.
1104 <https://doi.org/10.1029/2011JC007500>
- 1105 Tagliabue, A., Bopp, L., Dutay, J.-C., Bowie, A.R., Chever, F., Jean-Baptiste, P., Bucciarelli, E.,
1106 Lannuzel, D., Remenyi, T., Sarthou, G., Aumont, O., Gehlen, M., Jeandel, C., 2010.
1107 Hydrothermal contribution to the oceanic dissolved iron inventory. *Nat. Geosci.* 3, 252–256.
1108 <https://doi.org/10.1038/ngeo818>
- 1109 Tagliabue, A., Sallée, J.-B., Bowie, A.R., Lévy, M., Swart, S., Boyd, P.W., 2014. Surface-water
1110 iron supplies in the Southern Ocean sustained by deep winter mixing. *Nat. Geosci.* 7, 314–320.
1111 <https://doi.org/10.1038/ngeo2101>
- 1112 Tagliabue, A., Lough, A.J.M., Vic, C., Roussenov, V., Gula, J., Lohan, M.C., Resing, J.A.,
1113 Williams, R.G., 2022. Mechanisms Driving the Dispersal of Hydrothermal Iron From the
1114 Northern Mid Atlantic Ridge. *Geophys. Res. Lett.* 49. <https://doi.org/10.1029/2022GL100615>
- 1115 Tao, C., Guo, Z., Liang, J., Ding, T., Yang, W., Liao, S., Chen, M., Zhou, F., Chen, J., Wang, N.,
1116 Liu, X., Zhou, J., 2023. Sulfide metallogenic model for the ultraslow-spreading Southwest Indian
1117 Ridge. *Sci. China Earth Sci.* 66, 1212–1230. <https://doi.org/10.1007/s11430-023-1108-7>
- 1118 Tao, C., Li, H., Zhou, J., Wu, T., He, Y., Deng, X., Zhang, G., Liu, W., 2014. Seafloor
1119 hydrothermal activity and polymetallic sulfide exploration on the southwest Indian ridge.
1120 *Chinese Science Bulletin* 59, 2266–2276. <https://doi.org/10.1007/s11434-014-0182-0>
- 1121 Tao, C., Lin, J., Guo, S., Chen, Y.J., Wu, G., Han, X., German, C.R., Yoerger, D.R., Zhou, N.,
1122 Li, H., Su, X., Zhu, J., and the DY115-19 (Legs 1–2) and DY115-20 (Legs 4–7) Science Parties,
1123 2012. First active hydrothermal vents on an ultraslow-spreading center: Southwest Indian Ridge.
1124 *Geology* 40, 47–50. <https://doi.org/10.1130/G32389.1>
- 1125 Tao, C., Wu, G., Ni, J., Zhao, H., Su, X., Zhou, N., Li, J., Chen, Y., Cui, R., Deng, X., Egorov,
1126 I., Dobretsova, I., Sun, G., Qiu, Z., Zhou, J., Gu, C., Yang, J., Zhang, K., Wu, X., Lin, J., 2009.
1127 New hydrothermal fields found along the SWIR during the Legs 5-7 of the Chinese DY115-20
1128 Expedition. *AGU Fall Meeting Abstracts* 1150.
- 1129 Thomas, A.L., Henderson, G.M., Robinson, L.F., 2006. Interpretation of the ²³¹Pa/²³⁰Th
1130 paleocirculation proxy: New water-column measurements from the southwest Indian Ocean.
1131 *Earth Planet. Sci. Lett.* 241, 493–504. <https://doi.org/10.1016/j.epsl.2005.11.031>

- 1132 Thurnherr, A.M., Richards, K.J., German, C.R., Lane-Serff, G.F., Speer, K.G., 2002. Flow and
1133 Mixing in the Rift Valley of the Mid-Atlantic Ridge. *J. Phys. Oceanogr.* 32, 1763–1778.
1134 [https://doi.org/10.1175/1520-0485\(2002\)032<1763:FAMITR>2.0.CO;2](https://doi.org/10.1175/1520-0485(2002)032<1763:FAMITR>2.0.CO;2)
- 1135 Tonnard, M., Planquette, H., Bowie, A.R., van der Merwe, P., Gallinari, M., Desprez de
1136 Gésincourt, F., Germain, Y., Gourain, A., Benetti, M., Reverdin, G., Tréguer, P., Boutorh, J.,
1137 Cheize, M., Lacan, F., Menzel Barraqueta, J.-L., Pereira-Contreira, L., Shelley, R., Lherminier,
1138 P., Sarthou, G., 2020. Dissolved iron in the North Atlantic Ocean and Labrador Sea along the
1139 GEOVIDE section (GEOTRACES section GA01). *Biogeosciences* 17, 917–943.
1140 <https://doi.org/10.5194/bg-17-917-2020>
- 1141 van Beek, P., Bourquin, M., Reyss, J.-L., Souhaut, M., Charette, M.A., Jeandel, C., 2008.
1142 Radium isotopes to investigate the water mass pathways on the Kerguelen Plateau (Southern
1143 Ocean). *Deep Sea Res. Part II Top. Stud. Oceanogr.* 55, 622–637.
1144 <https://doi.org/10.1016/j.dsr2.2007.12.025>
- 1145 van Beek, P., Souhaut, M., Lansard, B., Bourquin, M., Reyss, J.-L., von Ballmoos, P., Jean, P.,
1146 2013. LAFARA: a new underground laboratory in the French Pyrénées for ultra low-level
1147 gamma-ray spectrometry. *J. Environ. Radioact.* 116, 152–158.
1148 <https://doi.org/10.1016/j.jenvrad.2012.10.002>
- 1149 van der Loeff, M.M.R., Moore, W.S., 1999. Determination of natural radioactive tracers, in:
1150 Grasshoff, K., Kremling, K., Ehrhardt, M. (Eds.), *Methods of Seawater Analysis*. Wiley-VCH
1151 Verlag GmbH, Weinheim, Germany, pp. 365–397. <https://doi.org/10.1002/9783527613984.ch13>
- 1152 Visbeck, M. (2002), Deep velocity profiling using Lowered Acoustic Doppler Current Profilers:
1153 bottom track and inverse solutions, *J. Atm. Ocean. Tech.*, 19, 794-807.
- 1154 Von Damm, K.L., 1990. SEAFLOOR HYDROTHERMAL ACTIVITY: BLACK SMOKER
1155 CHEMISTRY AND CHIMNEYS. *Annu. Rev. Earth Planet. Sci.* 18, 173–204.
1156 <https://doi.org/10.1146/annurev.ea.18.050190.001133>
- 1157 Walter, M., Mertens, C., Stöber, U., German, C.R., Yoerger, D.R., Sültenfuß, J., Rhein, M.,
1158 Melchert, B., Baker, E.T., 2010. Rapid dispersal of a hydrothermal plume by turbulent mixing.
1159 *Deep Sea Research Part I: Oceanographic Research Papers* 57, 931–945.
1160 <https://doi.org/10.1016/j.dsr.2010.04.010>
- 1161 Wolery, T.J., Sleep, N.H., 1976. Hydrothermal Circulation and Geochemical Flux at Mid-Ocean
1162 Ridges. *J. Geol.* 84, 249–275. <https://doi.org/10.1086/628195>
- 1163

1164 **Figure Caption:**

1165 **Table 1:** Radium activities at stations 14 and 15, “<DL” indicates activities below detection limit.
 1166 Here we report i) the Ra activity ratios determined in Mn-cartridges, ii) Ra activities determined
 1167 using Mn-fibers and iii) Ra activities in seawater determined by combining the ^{226}Ra activities
 1168 determined using Mn-fibers and the activity ratios determined using Mn-cartridges.

1169 **Table 2:** ^{227}Ac activities, in $\text{dpm } 100\text{L}^{-1}$, at stations 14 and 15.

1170 **Figure 1.** High resolution (15 m) bathymetry map of the SWIR segment investigated during
 1171 SWINGS cruise. The locations of stations 14 and 15 are shown as black triangles on the map. The
 1172 location of the segment is shown on the bottom left panel (black square). The color bar shows the
 1173 bathymetry that ranges from 862.8 to 2835.7 m.

1174 **Figure 2:** Temperature (grey full line), salinity (black full line), beam transmission (black dotted
 1175 line) and oxygen (grey dashed line) profiles at stations 14 (left panel) and 15 (right panel). The
 1176 horizontal black lines represent the bottom depth for each Station.

1177 **Figure 3.** Map of horizontal currents averaged between January 25 and January 29, 2021, from
 1178 satellite altimetry (a.) and from the GLORYS12 reanalysis at 190 m (b), 1250 m (c) and 1450 m
 1179 (d). The black line denotes the 2000 m isobath. The location of Stations 14 and 15 is indicated by
 1180 magenta triangles. Units in m s^{-1} .

1181 **Figure 4.** Horizontal currents at depths below 1000 m measured by the LADCP at station 14 on
 1182 28 January 2021 and at station 15 on 29 January. A second LADCP cast was performed at Station
 1183 14 on 28 January, denoted by thin arrows. Green arrows denote the barotropic tidal current at the
 1184 time of the cast according to the TPXO9v5 model. Corresponding variance ellipses for the
 1185 dominant M2 constituent computed between 27 January and 2 February are also shown. Current
 1186 velocity on 28 January from the GLORYS12 reanalysis are shown at a depth of 1250 m and 1450
 1187 m (where applicable): red dots denote model grid points. Bathymetry is from the multibeam echo
 1188 sounder (contour interval 50 m), with the 1250 m isobath highlighted. Unit for the velocity is cm
 1189 s^{-1} (velocity scale in the top right corner).

1190 **Figure 5.** $^{223}\text{Ra}_{\text{ex}}$ and $^{224}\text{Ra}_{\text{ex}}$ activities are shown as black circles and black triangles, respectively.
 1191 Filled symbols represent activities determined by combining the activities determined using Mn-
 1192 fibers and Mn-cartridges, while open symbols represent activities determined in the Mn-fibers.
 1193 The graph in the right panel in grey shows, as a comparison, the vertical profiles observed off
 1194 Kerguelen islands with grey triangle as $^{224}\text{Ra}_{\text{ex}}$ and grey dots as $^{223}\text{Ra}_{\text{ex}}$ (Sanial et al., 2015). Errors

1195 bars are reported but are often within the symbol. The horizontal lines represent the depth of the
1196 seafloor.

1197 **Figure 6.** ^{227}Ac activities are shown as black circles. The horizontal lines represent the depth of
1198 the seafloor.

1199 **Figure 7.** ^{226}Ra and ^{228}Ra activities are shown as white diamonds and black triangles, respectively.
1200 The horizontal lines represent the depth of the seafloor. Errors bars for ^{226}Ra are reported but are
1201 often within the symbol.

1202 **Figure 8.** Conceptual figure illustrating the circulation of the fluid within a hydrothermal system
1203 and the associated partitioning of radionuclides from the U-Th decay chain.

1204 **Figure 9.** Vertical eddy diffusivity coefficient (K_z) estimation at station 14 using a simple one-
1205 dimensional diffusion model applied to the vertical profiles of $^{223}\text{Ra}_{\text{ex}}$ (left panel) and $^{224}\text{Ra}_{\text{ex}}$ (right
1206 panel). The best exponential fits considering Ra data in the 1000–1250 m depth interval together
1207 with the R value are reported. The horizontal lines represent the depth of the seafloor. The
1208 uncertainties on the K_z are derived from the uncertainty on the best exponential fit coefficient of
1209 Ra activities as function of distance from bottom (Equation 2).